INVESTIGATION OF TiAlV AS ABSORBER AND WO_3-V_XO_Y AS ACTIVE MATERIAL FOR TERAHERTZ MICROBOLOMETERS

A THESIS SUBMITTED TO
THE GRADUATE SCHOOL OF NATURAL AND APPLIED SCIENCES
OF
MIDDLE EAST TECHNICAL UNIVERSITY

BY

BAHAR ATİK

IN PARTIAL FULFILLMENT OF THE REQUIREMENTS
FOR
THE DEGREE OF MASTER OF SCIENCE
IN
CHEMISTRY

JUNE 2022

Approval of the thesis:

INVESTIGATION OF TiAlV AS ABSORBER AND WO_3-V_XO_Y AS ACTIVE MATERIAL FOR TERAHERTZ MICROBOLOMETERS

submitted by **BAHAR ATİK** in partial fulfillment of the requirements for the degree of **Master of Science** i**n Chemistry, Middle East Technical University** by,

Prof. Dr. Halil Kalıpçılar
Dean, Graduate School of **Natural and Applied Sciences** _____

Prof. Dr. Özdemir Doğan
Head of the Department, **Chemistry** _____

Prof. Dr. Okan Esentürk
Supervisor, **Chemistry, METU** _____

Examining Committee Members:

Prof. Dr. Tayfun Akın
Electrical and Electronics Eng., METU _____

Prof. Dr. Okan Esentürk
Chemistry, METU _____

Prof. Dr. Hakan Altan
Physics, METU _____

Assoc. Prof. Dr. Mehmet Fatih Danışman
Chemistry, METU _____

Assoc. Prof. Dr. Dinçer Gökcen
Electrical and Electronics Eng., Hacettepe University _____

Date: 28.06.2022

I hereby declare that all information in this document has been obtained and presented in accordance with academic rules and ethical conduct. I also declare that, as required by these rules and conduct, I have fully cited and referenced all material and results that are not original to this work.

Name, Last Name: Bahar Atik

Signature:

ABSTRACT

INVESTIGATION OF TiAlV AS ABSORBER AND WO_3-V_XO_Y AS ACTIVE MATERIAL FOR TERAHERTZ MICROBOLOMETERS

Atik, Bahar
Master of Science, Chemistry
Supervisor: Prof. Dr. Okan Esentürk

June 2022, 81 pages

Terahertz technology continues to evolve rapidly from laboratory setups to commercial devices. The foreseen future of the THz technology has accelerated the fabrication of detectors that are sensitive in this frequency range. Current efforts for THz imaging applications have focused on using the mature microbolometer technology which has proven to be useful in the IR region. In microbolometers, the incoming radiation becomes absorbed in the absorber layer resulting in an increase in temperature. The electrical resistance of the active material layer changes with temperature, and the resultant resistance change is read by readout circuits. The objective of this thesis is to evaluate these two critical layers, absorber and active material layers, for THz microbolometer applications. For broadband THz imaging purposes, TiAlV thin film is investigated as the potential absorber layer. Owing to its lower conductivity compared to other metals and compatibility to microfabrication techniques, by tailoring the sheet resistance with control in layer thickness, significant enhancement in THz absorption is observed.

Here, the absorption of THz radiation will not increase the temperature as much as the more energetic IR waves. Hence, it is essential for a THz microbolometer to have a high temperature coefficient of resistance (TCR). For this purpose, the effect of V-W reactive co-sputtering is studied, and WO_3-V_xO_y is investigated as the potential active material layer. As the sputtering power of W increased, new phases appeared, and this has opened a pathway toward tuning the TCR of the film to a desired value by changing the characteristics of V_xO_y films. In addition, properties of V_xO_y and WO_3-V_xO_y layers are evaluated in the THz region as a function of temperature for the first time. Nondestructive characterization of these temperature sensitive materials gives a deep insight on their use in THz microbolometers.

Keywords: Terahertz, MEMS, Microbolometer, Absorber, Active Material

ÖZ

SOĞURUCU TiAlV VE AKTİF MALZEME WO_3-V_XO_Y'NİN TERAHERTZ MİKROBOLOMETRELER İÇİN İNCELENMESİ

Atik, Bahar
Yüksek Lisans, Kimya
Tez Yöneticisi: Prof. Dr. Okan Esentürk

Haziran 2022, 81 sayfa

Terahertz teknolojisi, laboratuvar kurulumlarından ticari cihazlara olan evrimine başlamıştır. THz teknolojisinin öngörülen geleceği, bu frekans aralığında hassas detektörlerin üretimini motive etmiştir. THz görüntüleme uygulamaları için mevcut çabalar, Kızılötesi bölgede başarılı olduğu kanıtlanmış mikrobolometre teknolojisini kullanmaya odaklanmıştır. Mikrobolometrelerde, gelen radyasyonun soğurucu katmandaki emilimi sonucunda sıcaklıkta artış meydana gelir. Aktif malzeme katmanının elektriksel direnci sıcaklığa bağlı olarak değişir ve ortaya çıkan direnç değişikliği, okuma devreleri tarafından okunur. Bu tezin amacı, THz mikrobolometre uygulamaları için bu iki kritik katmanı, soğurucu ve aktif malzeme katmanlarını değerlendirmektir. Geniş bant THz görüntüleme uygulamaları için TiAlV ince filmler potansiyel THz soğurucu katman olarak incelenmiştir. Diğer metallere göre daha düşük iletkenliği ve mikrofabrikasyon yöntemlerine uygunluğu sayesinde, katman kalınlığı kontrollü olarak tabaka direncine uyarlanarak, THz soğurmada önemli bir artış gözlemlenmiştir.

THz dalgalarının soğurulması, daha yüksek enerjili Kızılötesi dalgalarının soğurulması kadar fazla bir sıcaklık artışına neden olmayacaktır ve dolayısıyla bir THz mikrobolometrenin yüksek sıcaklık direnç katsayısına (TCR) sahip olması büyük önem taşımaktadır. Bu amaçla, V-W reaktif eş zamanlı saçtırmanın etkisi araştırılmış ve WO_3-V_xO_y potansiyel aktif malzeme katmanı olarak değerlendirilmiştir. W metaline uygulanan saçtırma gücü artırıldıkça yeni fazlar ortaya çıkarak V_xO_y filmlerin özelliklerini önemli ölçüde değiştirmiş ve TCR değerini istenen bir değere yükseltmeye olanak sağlamıştır. Ayrıca, V_xO_y ve WO_3-V_xO_y katmanlarının özellikleri, THz bölgesinde sıcaklığın bir fonksiyonu olarak ilk kez değerlendirilmiştir. Sıcaklığa duyarlı bu malzemelerin tahribatsız karakterizasyonu, THz mikrobolometrelerdeki kullanımları hakkında önemli sonuçlar vermiştir.

Anahtar Kelimeler: Terahertz, MEMS, Mikrobolometre, Soğurucu Katman, Aktif Malzeme

To the journey…

ACKNOWLEDGMENTS

I would like to express how grateful I am to my supervisor Prof. Dr. Okan Esentürk for his supervision, support, and invaluable guidance starting from my undergraduate years. It will always be an exceptional opportunity to work with him.

I would like to thank Prof. Dr. Hakan Altan for his valuable comments and suggestions not only for this study but also for this period of my life. I would also like to thank Prof. Dr. Tayfun Akın for sharing his immense knowledge with me throughout my years at METU MEMS Center.

I would like to thank all my colleagues at METU MEMS Center for the friendly work environment. I would like to thank Dr. Mustafa Yıldırım firstly for the ideas he provided for this study, and more essentially for his continuous support. I would like to express how lucky I feel to have met and worked with Orhan Akar, his vast experience and knowledge has shaped my thoughts and guided my processes in cleanroom. I would like to thank Emrah Dirican, for not only his help with the XPS analysis, but also for the long hours spent together in cleanroom, and for the conversations full of laughing. I would also like to thank Oytun Demirörs for his joyful friendship both at and outside work. I would like to express my gratefulness to Murat Artuç, Utku Çekmez, and Baran Utku Tekin for their help with the noise data. It is their kind help and support that have made my study and experience at METU MEMS Center a wonderful time.

Last but not least, it may sound like a cliché but the greatest thanks goes to my mother Dilek Sakarya and to my father Cüneyt Atik for always being there for me, for the endless support they provided, and for believing in me no matter what. I would finally like to thank Miraç Eroğlu for his incredible patience. This thesis could not have been written without his encouragement and support.

This work is partially funded by TÜBİTAK under grant number 120F067.

TABLE OF CONTENTS

LIST OF TABLES

TABLES

LIST OF FIGURES

FIGURES

CHAPTER 1

INTRODUCTION

Terahertz (THz) region has remained unexplored for a long time, with the exception of applications in astronomy. Now, with recent technological developments in micro and nanotechnology, various MEMS structures are being developed for the THz region. One of them is the microbolometer structure which is a thermal detector being utilized for imaging purposes. Since THz waves can penetrate through clothing or widely used packaging materials, imaging in the THz region enables one to see through these materials nondestructively. Furthermore, the non-ionizing nature of THz waves makes them a safe alternative to X-rays and opens a pathway for biomedical imaging applications as well. These advantages of using THz waves for imaging purposes had led many researchers to optimize the widely used Infrared (IR) microbolometer structures for the THz region. Following sections of this chapter give comprehensive information about the THz region and the microbolometer technology. Section 1 introduces THz waves in the electromagnetic spectrum and explains the interactions of them with different materials highlighting the importance of using THz waves in imaging applications. Section 2 introduces the microbolometer technology briefly. Section 3 summarizes the efforts on using IR microbolometers in the THz region with examples from the literature, while Section 4 states the objectives of this thesis and the organization.

1.1 THz Region

The term “Terahertz” originates from the unit prefix “Tera” which stands for 10^{12}, so that 1 THz equals 10^{12} Hertz. To mention briefly, 1 THz corresponds to a wavelength of 300 μm, a wave number of 33 cm^{-1}, a photon energy of 4.1 meV which equals to $6.57x10^{-22}$ Joules, and temperature of 47 K.[1, 2] Although the lower and upper limits of this frequency range vary in different resources, they are generally accepted as 0.1 THz (100 GHz) to 10 THz.[3] This frequency range lies in between Microwave and Infrared regions in the electromagnetic spectrum as shown in Figure 1.1.

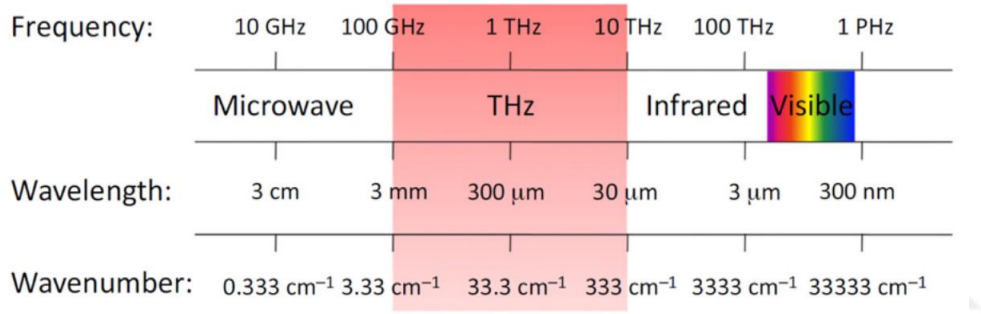

Figure 1.1. The THz region in the electromagnetic spectrum.[4]

At this frequency range, electromagnetic waves have unique interactions with materials. These low energy THz waves can pass through most nonconductive materials e.g., plastic, paper, and fabric whereas they are highly reflected from conducting bulk materials.[5] Therefore, most attractive application areas are nondestructive inspection and security imaging since THz waves can be used to detect knives, guns, and explosives hidden in packages or under clothes by providing a vision through camouflage.[6] Besides, since water has strong absorption characteristics at this frequency range, THz waves can also be used to determine water and moisture content of a sample.[7] Key strength of THz is that, unlike X-rays, it is nonionizing and is therefore a safer choice for medical imaging without causing any harm on living things.[8, 9]

With these advantages, potential application areas are widened in years, and the predicted future of the THz technology has motivated the production of sensitive THz detectors for imaging purposes. Since THz waves have a wide range of application areas from medical imaging, quality control, security, and food inspection, to even remote sensing of landmines, real-time imaging with compact sensors is highly desirable which can be achieved by using the microbolometer technology.

1.2 Microbolometer Technology

MEMS-based microbolometer technology provides small, low-cost, lightweight, and uncooled sensors that work at room temperature. This technology has proved its potential in real-time imaging in the IR region for many years.[10] A microbolometer is a thermal sensor which works in such a way that the incoming radiation which is absorbed in the absorber layer results in an increase in temperature. This temperature increase changes the electrical resistance of the active material layer which contains a temperature sensitive material. Mixed phase vanadium oxides (V_xO_y) are the most widely used temperature sensitive materials in commercial IR microbolometers followed by amorphous silicon (a-Si).[11] The resultant resistance change is then read by readout circuits. A simple schematic demonstration of one pixel in a microbolometer structure is given in Figure 1.2.

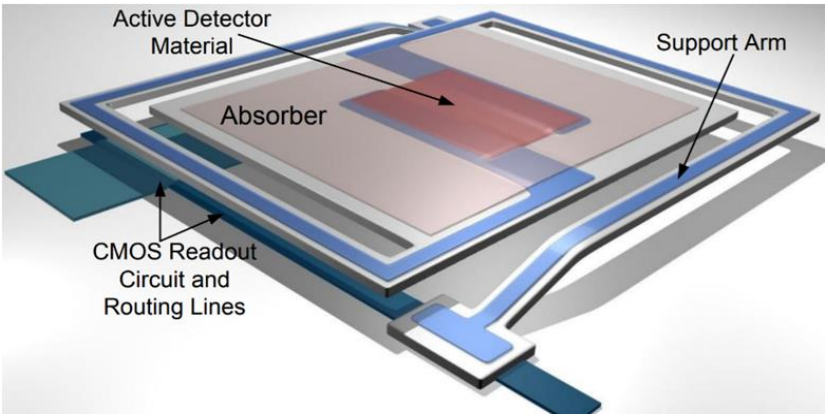

Figure 1.2. Microbolometer pixel structure showing critical components.[12]

These pixel structures come together to form focal plane arrays (FPAs) which are the assembly of individual pixel structures in an array format at the focal plane of the lens in the imaging system.

SEM images of several V_xO_y microbolometer pixel structures produced by different companies for the IR region are given in Figure 1.3.

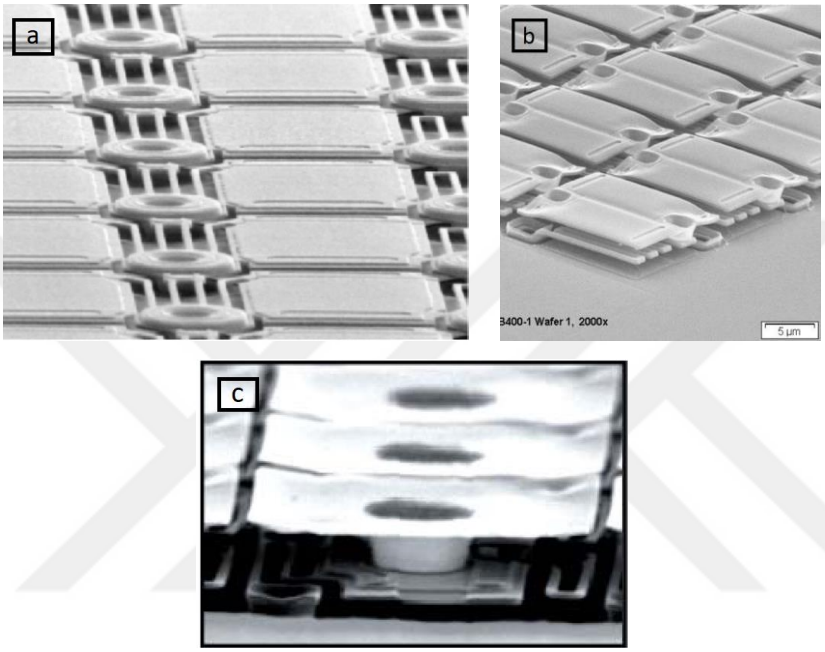

Figure 1.3. V_xO_y microbolometer FPA a) with 28 µm pixel pitch by BAE Systems [13], b) with 17 µm pixel pitch by Raytheon [14], and c) with 17 µm pixel pitch and umbrella design by DRS [15].

BAE Systems, DRS, Raytheon, SCD, FLIR, and NEC are some of the leading companies that utilized V_xO_y as the microbolometer active material.[16] Recently, the pixel size is being reduced with advanced improvements in the IR microbolometer technology. Today, commercial IR microbolometers usually have 17 µm or 12 µm pixel pitches.

BAE systems offers a full high-definition Infrared imaging with Athena1920 having a 12 µm pixel pitch utilizing V_xO_y microbolometer. DRS has reduced the pixel pitch to 10 µm in their product Tenum640. Furthermore, world's first 8 µm IR microbolometer is announced by InfiRay in 2021.

Although the reduced pixel pitches might not be convenient for THz waves since they have much longer wavelengths than IR waves, the know-how acquired in the IR region is being widely used for the THz region. Starting point is to try the mature IR microbolometer technology in the THz region as it is, and then to optimize it for state-of-the-art THz imaging.

1.3 Imaging in THz Region with Microbolometers

Real-time imaging at THz frequencies is shown to be achieved by using the mature IR microbolometer technology by various research groups and companies. These studies will be discussed thoroughly in this section. Although there are several studies demonstrating a real-time imaging at THz frequencies by using THz emission sources i.e., Terahertz quantum-cascade lasers (THz-QCLs), detectors are mostly designed for the IR region.

The first reported use of existing 7.5-14 μm IR microbolometer FPA technology for the THz region is performed by Lee *et al*. in a study which successfully demonstrates the use of a commercial uncooled IR microbolometer FPA camera (SCC500L, BAE Systems) for real-time THz imaging.[17] A far-infrared gas laser (2.52 THz) having an approximately 10 mW output power is used as the THz source. The IR microbolometer camera uses 320x240 array with pixel pitches of 46.25 μm having V_xO_y as the active material, and it is optimized for the wavelength range of 7.5-14 μm. Even though the FPA is not optimized for THz wavelengths, it shows sensitivity at 2.52 THz and could see the razor blade placed inside a FedEx envelope. Another study by Lee *et al*. shows real-time THz imaging using again the detector SCC500L from BAE Systems, but this time with a 4.3 THz-QCL having a 50 mW peak power as the illumination source.[18] The performance of the detector is evaluated in terms of optical noise equivalent power (NEP) which defines the incident optical power needed to achieve a signal-to-noise ratio (SNR) of 1. Lee *et al*. shows that the optical NEP of the microbolometer FPA at 4.3 THz is estimated to be 320 $pW/Hz^{1/2}$.

A similar study by Oda *et al*. shows the use of a 3.1 THz-QCL as the illumination source and different V_xO_y IRFPA configurations, namely 320x240 array with pixel pitches of 37 μm, 320x240 array with pixel pitches of 23.5 μm, and 640x480 array with pixel pitches of 23.5 μm, as detectors.[19] Using these THz-QCL and IRFPAs, measured NEP values are in the range of 200-300 pW/Hz$^{1/2}$, which are comparable with the 320 pW/Hz$^{1/2}$ NEP value obtained in the previously explained study by Lee *et al*. For improvement in the THz region, authors have replaced the Ge window of the vacuum package with a high-resistive Si window having both sides coated with antireflective Parylene for near unity THz transmission through the window. The detailed transmission profiles with different antireflecting coatings are presented in another study by Naoki Oda.[20] In addition to this material change, authors improved the NEP to 40 pW/Hz$^{1/2}$ by adding a thin metallic THz absorber layer (specified as TiAlV at Ref [20]) on top of the 320x240 array with two-floored 23.5 μm pixel structures shown in Figure 1.4.

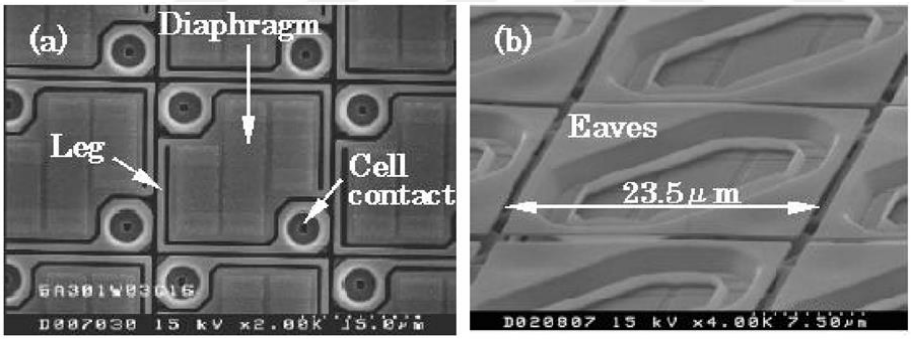

Figure 1.4. SEM images of the a) first and b) second floor of 23.5 μm pixels fabricated by NEC.[19]

Another similar study by Gou *et al*. uses 320x240 V_xO_y microbolometer IRFPA with pixel pitches of 37 μm having a NiCr layer as the absorber layer.[21]

The study shows the use of reactive ion etching (RIE) on the dielectric support layer underneath the NiCr layer to increase its effective surface area by creating nanoscale surface structures caused by RIE. The as-deposited and RIE-treated NiCr layers on top of pixel structures are compared, and it is concluded that RIE-treated films have an enhanced absorption in THz region.

In another study again by Gou *et al*., a 2.52 THz far-infrared gas laser is used as the source and V_xO_y microbolometer FPA having 320x240 array with pixel pitches of 35 μm as the detector.[22] This time, the authors have deposited Ti film having 20 nm of thickness and reduced its thickness to 9 nm again by performing RIE to improve the THz absorption. The resulting NEP obtained is 45.7 pW/Hz$^{1/2}$ which is comparable with the NEP value in the previous study by Oda *et al*. which was 40 pW/Hz$^{1/2}$. Another study by Nemoto *et al*. shows that the sensitivity can be improved with a SiN layer deposited on the mirror layer of the microbolometer structure to increase the effective cavity length for THz waves.[23] In that study, instead of using NEP, authors defined the minimum detectable power (MDP) as the THz wave power when SNR is equal to 1. By increasing the cavity length with the inserted SiN layer, MDP is improved by about one order of magnitude below 1 THz.

These studies show that using the current IR V_xO_y microbolometer technology in the THz region shows promising results. Experiments on available IRFPAs under THz illumination sources show NEP values around 200-300 pW/Hz$^{1/2}$. On the other hand, with simple efforts on enhancing the THz absorption by inserting a THz absorber layer and/or changing the vacuum package window materials, it is possible to improve NEP values to around 40 pW/Hz$^{1/2}$ and even lower with specific cavity length modifications for THz waves.

It is also worth mentioning that all the studies use “active imaging” by utilizing an illumination source for imaging. In a “passive imaging” case, the real-time imaging is achieved without an illumination source where objects are emission sources themselves. Detecting the thermal radiation of room temperature objects is a difficulty for the THz region because of the low thermal radiation of room temperature objects in the THz region, especially compared to the IR background. Passive imaging in the THz region is thus a challenge by requiring NEP values in the fW (10^{-15}) range instead of the pW (10^{-12}) range [24].

NEC, CEA-LETI, and INO have manufactured microbolometers that are modified for THz frequencies. THz-optimized detectors manufactured by these companies are listed in the Table 1.1 where they all are based on the uncooled microbolometer FPA technology. In addition to these, the company i2s also has a THz microbolometer product named TZcam which uses the patented design of CEA-LETI.

Table 1.1. Various uncooled microbolometer FPA based THz detectors manufactured by different companies.

Company (product)	*Type of detection*	*Pixel pitch*	*Frequency Range*	*#of pixels*	*Ref*
NEC (IRV-T0831)	V_xO_y FPA	23.5 μm	1-7 THz	320x240	[25]
CEA-LETI (TZcam)	Antenna coupled a-Si FPA	50 μm	0.3-5 THz	320x240	[26]
INO (IRXCAM-THz-384)	V_xO_y FPA	35 μm	0.094-4.25 THz	384x288	[27]

It is worth mentioning that TeraSense is one of the leading companies that manufacture components for real-time THz imaging. Detectors produced by TeraSense are based on a patented GaAs technology utilizing plasmonic oscillations for confining THz waves which are not involved in the scope of this thesis. It should be noted that all the improvements using various technologies and techniques contribute to the promising future of real-time THz imaging. In the "Roadmap of THz Imaging 2021," Valušis *et al*. state that there is a promising development trend in the MEMS-based microbolometer technology.[28] There is still room for reaching state-of-the-art THz microbolometers.

1.4 Scope and Organization of the Thesis

The main goal of this thesis is to evaluate specific properties of promising materials and to optimize them to be used in absorber and active material layers of future THz microbolometers. Although the microbolometer technology is being widely used as a mature technology in the Infrared region, it still needs optimizations to be used in the THz region.

Firstly, room temperature objects emit maximum at Infrared region, so the amount of the THz radiation emitted from objects at room temperature are far more less than the amount of Infrared radiation. In addition to that, THz waves are also less energetic than Infrared waves. Therefore, one will not only have a less amount of the incoming radiation but also a less energetic radiation while considering imaging in the THz region. The temperature change that will be created by this less amount of less energetic waves is challenging to sense compared to the temperature increase that Infrared causes. By taking those limitations into consider, there are two layers that need careful optimization. First layer is the absorber layer. Since there is no room for losing any of the incoming light, the absorber of a THz microbolometer should be optimized to absorb maximum while considering the trade-off between other important parameters such as sheet resistance and thickness. Second layer to be optimized is the active material layer. The absorption of THz radiation will not cause a temperature increase as much as the more energetic Infrared waves. Therefore, the temperature coefficient of resistance (TCR), the change in resistance with a unit change in temperature, should be as large as possible for the active material to cause a significant resistance change even with the slightest temperature change while considering the trade-off between TCR and noise. In this thesis, to point the requirements for imaging with a microbolometer in the THz region, these two critical layers i.e., absorber and active material layers, and their various properties are investigated in detail.

Absorber and active material layers are studied not only using conventional characterization techniques but also using THz Time Domain Spectroscopy (THz-TDS) to understand these materials in the THz region by a nondestructive characterization with THz-TDS.

In Chapter 1, the THz region and the microbolometer technology are first introduced separately. The motivation of using the microbolometer technology in the THz region and required improvements are then explained with examples from the literature.

Chapter 2 focuses on the absorber layer using a titanium alloy, TiAlV. The fabrication method is presented in detail, and it is followed by electrical and THz optical characterizations.

The effect of the film thickness on the absorption, sheet resistance, and foreseen speed of the detector is discussed in Chapter 2. The trend in the absorption behavior with varying sheet resistances is compared with the literature and experimental sheet resistance values are confirmed with THz-TDS measurement results.

Chapter 3 investigates the effect of reactive co-sputtering of Vanadium (V) and Tungsten (W) in an Argon/Oxygen environment. The resulting V_xO_y and WO_3-V_xO_y films fabricated by applying different sputtering powers to W target are evaluated from different aspects utilizing structural, electrical, and THz optical characterization techniques. Here, co-sputtering of V and W is explained in detail as a method to adjust TCR and relative phase concentrations. These effects of V-W co-sputtering are also monitored using THz-TDS for the first time in the literature.

Finally, Chapter 4 summarizes the results of this thesis and defines the future work based on these results.

CHAPTER 2

ABSORBER LAYER

2.1 Material of Choice, TiAlV

A titanium alloy, TiAlV, is investigated as the potential THz absorber layer. Unfortunately, the widely used IR absorber layer NiCr cannot reach high THz absorption values.[21] By using density and specific heat values of TiAlV and NiCr given in Table 2.1, a simple calculation is performed to compare the number of photons required to increase the temperature of both 10 nm TiAlV and NiCr layers. To increase the temperature of a 10 nm TiAlV layer by 1 K, 1.7×10^{-7} J of energy is required, while this number is 2.6×10^{-7} J for a NiCr layer. Then, approximately 30 times more photons are needed to increase the temperature of a 10 nm NiCr layer by 1 K with 300 μm THz waves (6.57×10^{-22} J/photon) instead of 10 μm IR waves (1.99×10^{-20} J/photon) since THz waves are much less energetic. On the other hand, number of photons needed to increase the temperature of the absorber layer by 1 K will decrease by 1.5 times when 10 nm TiAlV is used as the absorber layer rather than NiCr. Its lower density is a significant advantage also for the fabrication of thicker TiAlV absorber layers without increasing the mass as much as NiCr. Another important advantage of TiAlV is its higher electrical resistivity (lower electrical conductivity) since THz waves are likely to be reflected from electrically conductive surfaces. Its lower conductivity might help minimizing these reflection losses. This is also the reason for choosing TiAlV alloy instead of Ti itself, because there is a significant difference in their electrical resistivity values. (Table 2.1)

Table 2.1. Properties of TiAlV, Ti, and NiCr for comparison.

	TiAlV	**Ti**	**NiCr**	**unit**
Thermal Conductivity	7.2	21.9	15	$Wm^{-1}K^{-1}$
Density	4.42	4.5	8.3	g/cm^{3}
Specific Heat	0.56	0.54	0.44	$Jg^{-1}K^{-1}$
Electrical resistivity	1.7	0.4	1.1	$10^{-6}\ \Omega m$
Thermal expansion	8.7	8.6	14	$10^{-6}/K$

Considering all the above-mentioned issues, TiAlV is chosen as the candidate absorber layer for THz microbolometers. Indeed, TiAlV is the simplified version of "Ti-6Al-4V". These numbers in its widely known name "Ti-6Al-4V" indicate the weight percentage of individual elements in the alloy i.e., 90% Ti, 6% Al, and 4% V by weight. Ti-6Al-4V alloy is the most widely used alloy of titanium in the industry.[29] When pure titanium is heated above its phase transition temperature, it undergoes an allotropic transformation from its α phase to its β phase which are shown in Figure 2.1. Alloying elements added to pure titanium can stabilize the α phase by increasing the phase transition temperature, as well as stabilize the β phase by lowering this temperature. Aluminum in Ti-6Al-4V alloy is an "α" stabilizer, while vanadium is a "β" stabilizer, which makes Ti-6Al-4V alloy a two-phase "α + β alloy".[30]

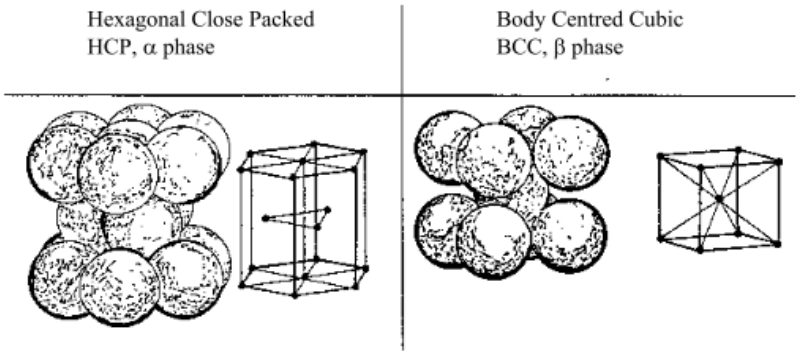

Figure 2.1. Two structural phases of Ti-6Al-4V.[31]

One of the most important things to consider when working with this alloy is that Titanium has a great binding affinity for oxygen (also an α stabilizer).[32] This is an essential issue to consider in electrical measurements of TiAlV thin films after their fabrication in vacuum. Electrical resistance of thin films will increase after a while since the surface will be oxidized when exposed to the atmosphere. This effect is further investigated in the Section 2.4.

2.2 Fabrication and Thickness Measurements

The fabrication of the absorber layer is achieved by using DC magnetron sputtering technique in a high vacuum (10^{-7} Torr) deposition chamber (AJA INTERNATIONAL, Inc.). Sputtering is a widely used Physical Vapor Deposition (PVD) technique for thin film fabrications.[33] It utilizes a plasma containing non-reactive ions i.e., Ar^+ in most of the cases since it will not form any compounds with the target material and not affect the deposited thin film composition. Ar^+ ions are accelerated toward the negatively charged cathode where the target material is placed. They will remove atoms and molecules from the surface of the target material physically. The removed atoms will follow a path until they encounter another atom, molecule, or a surface. The substrate to be coated is placed in their path so that the target material is deposited on the surface of the substrate.

TiAlV absorber layer fabrications are started with the optimization of process parameters. First deposition trials are made on Si substrates on which photoresist was patterned to measure the deposited film thickness with the surface profilometer after the lift-off process. The preparation of these Si substrates is a single lithography process. Lithography itself generally consists of three main steps as schematically shown in Figure 2.2 with both cross-section and top views.

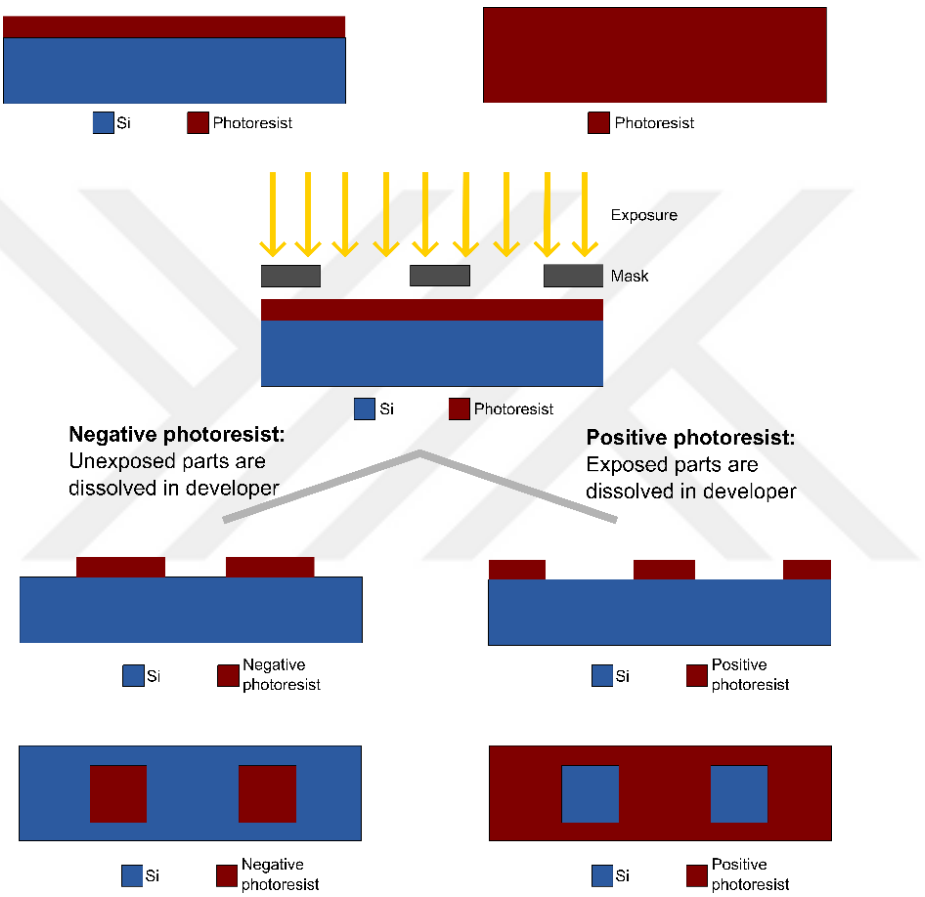

Figure 2.2. Three main steps of the lithography depending on the type of the photoresist with cross-section and top views.

The first step is the spin coating of the primer solution hexamethyldisilazane (HMDS) which is used to provide a good adhesion between the photoresist and the substrate. This step is followed by coating the photoresist, which is a photosensitive material, on the HMDS coated substrate. The coated photoresist is then soft baked and exposed to UV over the desired mask in the second step.

The third and the final step is dissolving the photoresist parts that are exposed or not exposed to UV in a chemical solvent called “developer”. The chemical dissolution behavior varies according to the photoresist type being positive or negative [34], and both cases are shown in Figure 2.2.

Throughout this absorber layer chapter, AZ5214E photoresist is used in the “image reversal” mode to exhibit negative behavior. AZ5214E is indeed a positive photoresist but is commonly used in the image reversal mode to obtain a negative image of the mask pattern with high resolution.[35] Patterning an image reversal photoresist includes the steps shown in Figure 2.3.

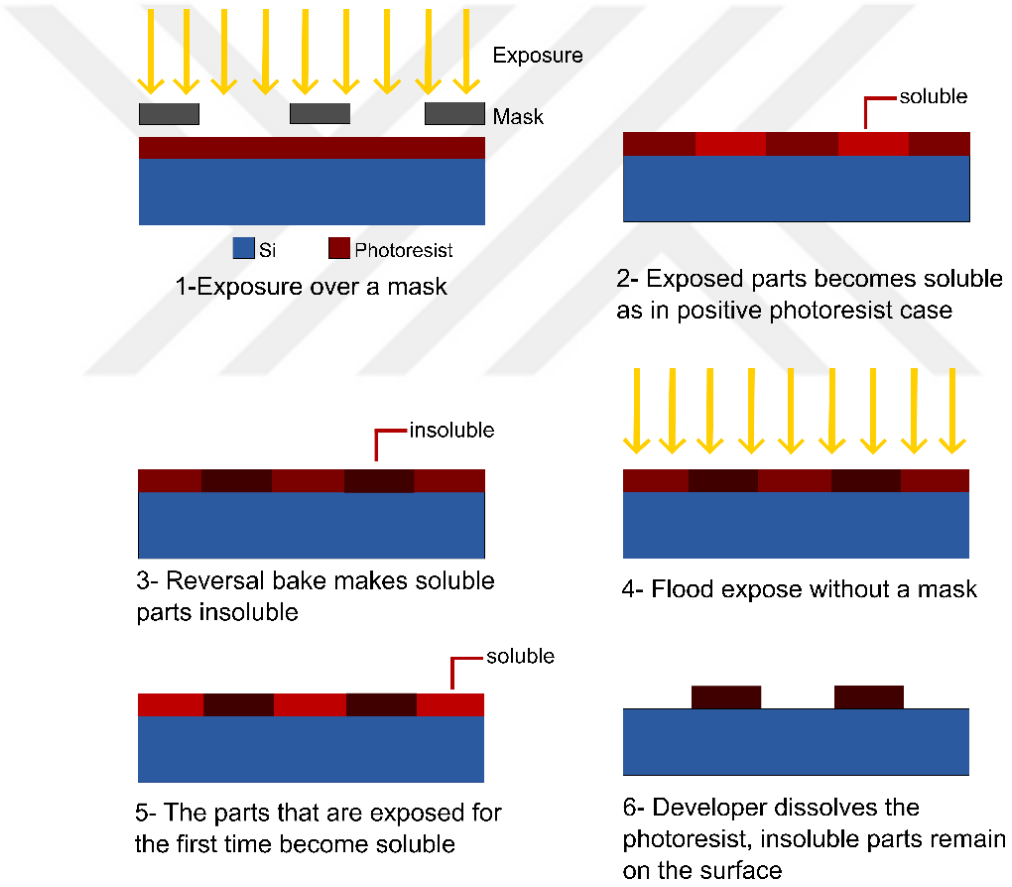

Figure 2.3. Process steps for performing AZ5214 lithography in an image reversal mode.

It starts with spin coating of the primer HMDS and photoresist i.e., AZ5214E, followed by UV exposure over a mask, as the first two main lithography steps explained above. The image reversal part starts after the first exposure. The process continues with “reversal bake” in this case. The exposed and normally soluble part of the photoresist forms crosslinks during the bake, which makes it insoluble in the developer at the final step. Reversal bake is followed by the second UV exposure called “flood expose” which is performed without a mask. Since unexposed parts from the first exposure are exposed to UV for the first time in this step, they become soluble in the developer now. After they are dissolved in the developer, the resulting pattern is the negative image of the mask, achieved by using a positive photoresist in an image reversal mode.

After creating a photoresist pattern on the surface of the Si substrate by lithography, the next step is to deposit TiAlV on this patterned surface. One approach to deposit a compound of thin film is co-sputtering of individual elements simultaneously. However, it is challenging to control the exact amounts of each element and obtain Ti-6Al-4V weight ratios precisely. Therefore, we have used a commercial compound target for Ti-6Al-4V alloy (Lesker, 99.9%).

To ensure plasma stability during TiAlV sputtering, voltage and current values are monitored by changing process parameters such as the power applied to the cathode, process pressure, and Argon gas flow. It is clearly observed that starting the process at higher pressures can help significantly while igniting the plasma for the first time. The process pressure can then be lowered to the desired value, once the voltage and current values and consequently the plasma are stable. After obtaining the plasma stability, a recipe is written that can maintain the plasma stability for a long period. The first step of this two-step recipe is to provide Argon flow into the deposition chamber. When the deposition chamber reaches a sufficient gas saturation after 5 minutes, power is applied to the cathode and the plasma is formed. After the shutter of the TiAlV target is opened, the second and the main step, the deposition starts and continues for a desired duration.

Once the TiAlV deposition is completed, the process continues with the lift-off step. The lift-off process removes the photoresist patterns formed in the lithography step together with the TiAlV layer deposited on them. This process takes place in an acetone bath. Samples that are in the acetone bath are cleaned using an ultrasonic bath. Finally, TiAlV that does not have photoresist underneath remains on the substrate surface, with the desired mask pattern, while TiAlV that has photoresist underneath is removed from the surface together with the photoresist. The cross-sectional schematic view of a Si substrate after each process step starting from the lithography (image reversal) to TiAlV deposition and lift-off steps are shown in Figure 2.4.

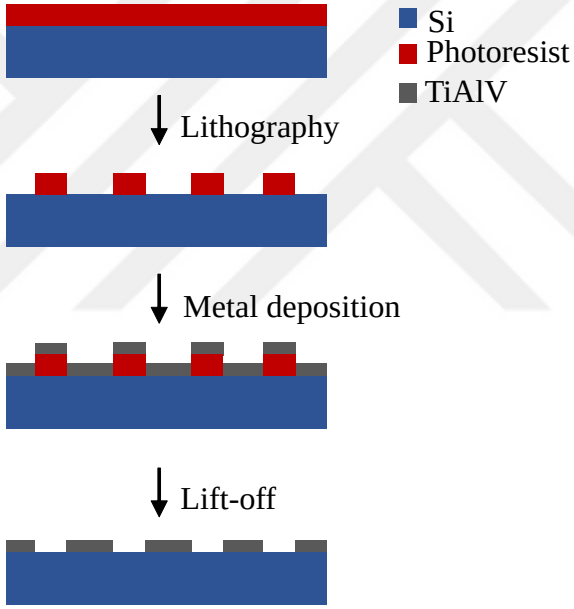

Figure 2.4. Fabrication steps of TiAlV patterns on Si substrates for thickness measurements.

The mask used in the lithography step is chosen to be suitable for thickness measurements. Simple TiAlV patterns created for thickness measurement purposes are shown in Figure 2.5. Thickness measurements are performed using DEKTAK surface profilometer on these patterns.

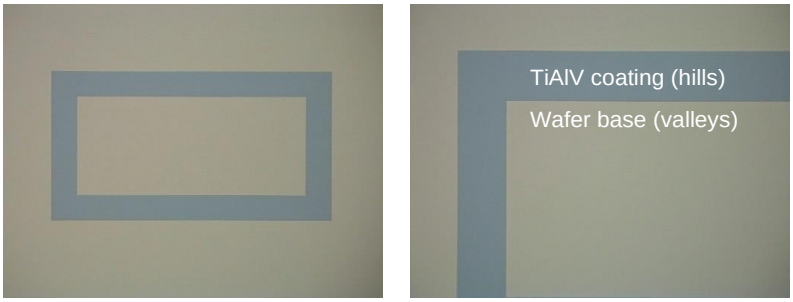

Figure 2.5. Optical microscope images of TiAlV thickness measurement patterns.

After measuring the thickness of the first trial sample, and the deposition rate is determined, following depositions are performed targeting 80 nm, 40 nm, and 20 nm of TiAlV thicknesses. After these depositions, actual thicknesses are measured as 85 nm, 39 nm, and 22 nm, respectively.

It is shown in Figure 2.6 that there is a linear relationship between the thickness and the deposition time for this thickness interval. Depositions are then performed targeting specific thicknesses with the latest deposition rate calculated from the most recent deposition.

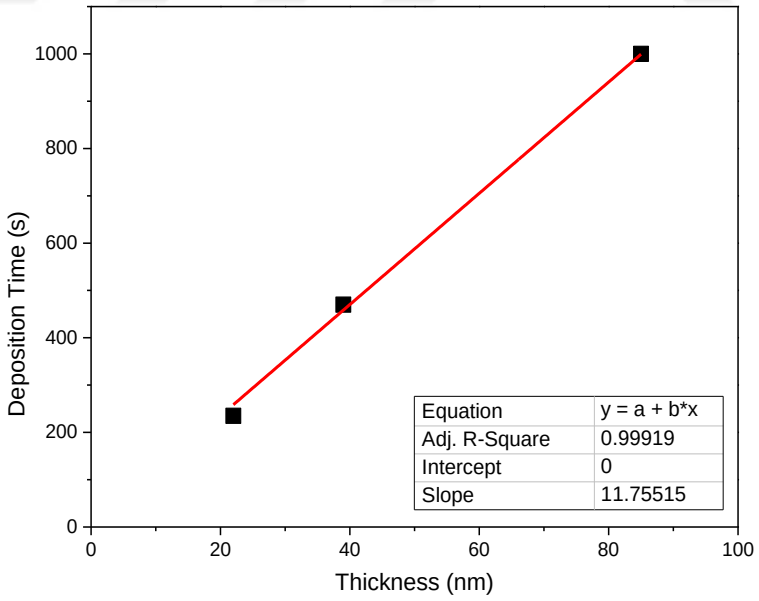

Figure 2.6. TiAlV layer thickness with varying deposition time.

2.3 SEM-EDX

In the fabrication of TiAlV thin films, a compound target “Ti-6Al-4V” is used for the sputtering. Elemental ratios in these films fabricated by the DC magnetron sputtering technique are determined by several SEM-EDX (Hitachi) analyses from the cross-section of TiAlV layer and not from the surface to eliminate the potential background signals that will arise from the layers below TiAlV. Figure 2.7 shows the cross-section SEM image of the TiAlV film deposited on the Si substrate and three points where EDX spectra are collected from. Three EDX spectra points are indicated as Spectrum 1, 2, and 3 in Figure 2.7a. Figure 2.7b shows Spectrum 1 which is the EDX spectrum from the point on the Si substrate. The EDX spectrum showed 98.5% Si for the substrate as expected. Spectrum 2 shown in Figure 2.7c is from the interface of Si and TiAlV, the EDX results are thus 74.1% Ti, 15.8% Si, 6.6 % Al, and 3.5% V, which are reasonable percentages for the interface. The last one, Spectrum 3 in Figure 2.7d is entirely from the TiAlV layer, ratios obtained from the EDX analysis are 88.7% Ti, 6.9% Al, and 3.8% V, and they are compared with the original ratios of the target material in Table 2.2. It is observed that elemental ratios of the deposited film and the target material are compatible.

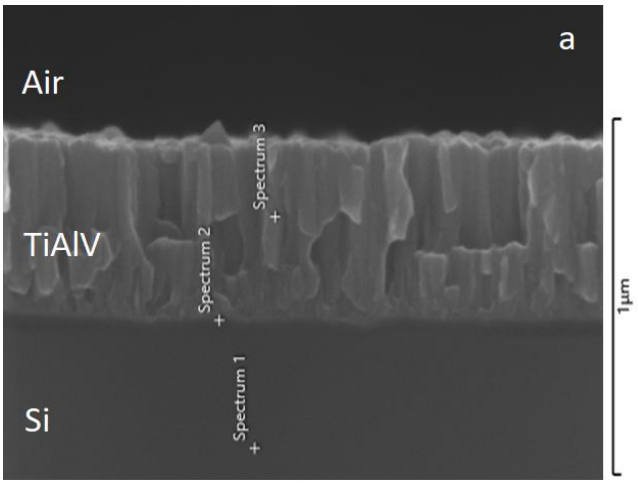

Figure 2.7. a) Cross-section SEM image of the TiAlV deposition; EDX spectrum corresponding to the b) Si substrate, c) interface between Si substrate and TiAlV, and d) TiAlV layer itself.

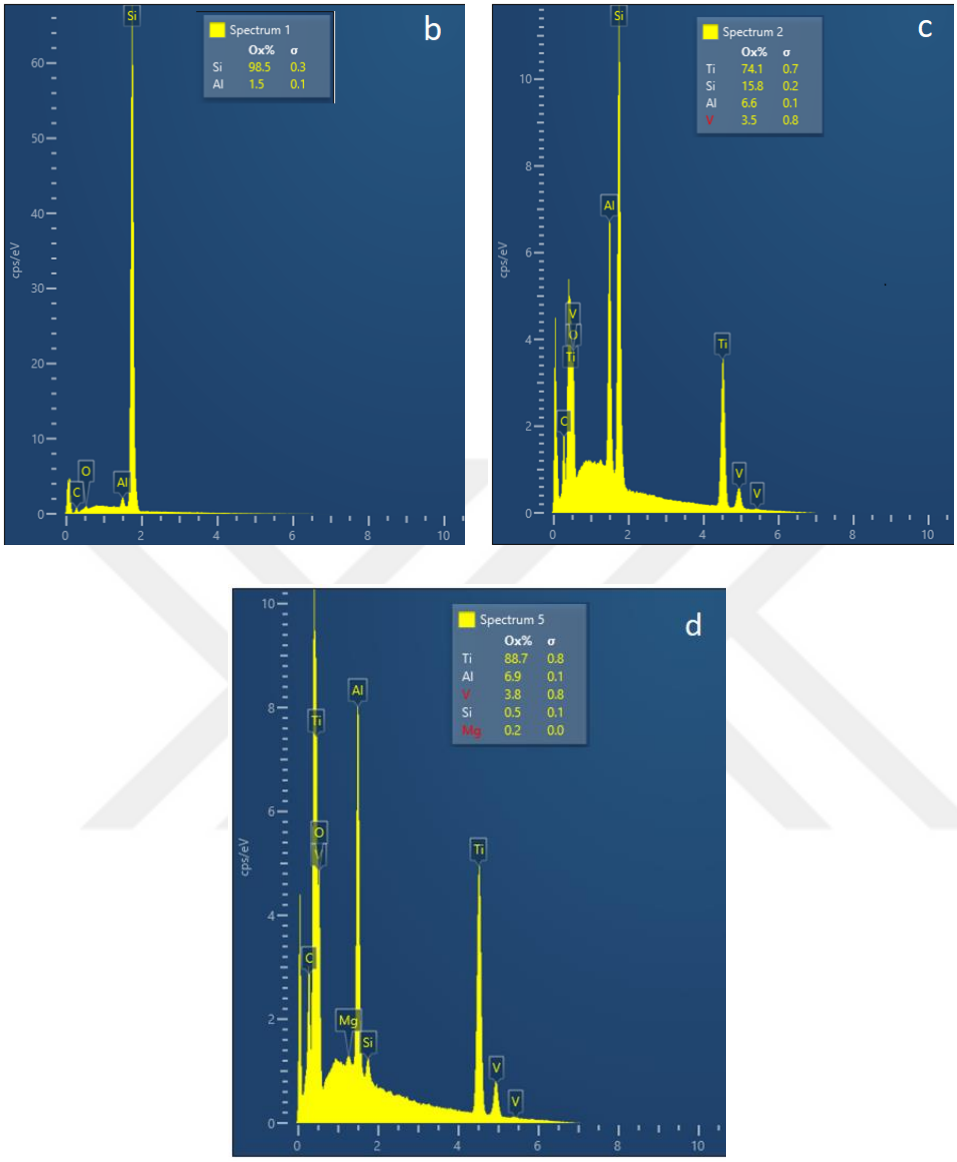

Figure 2.7 (continued). a) Cross-section SEM image of the TiAlV deposition; EDX spectrum corresponding to the b) Si substrate, c) interface between Si substrate and TiAlV, and d) TiAlV layer itself.

Table 2.2. Elemental ratios in the original target and the deposited TiAlV film.

Element	Ratio in the commercial target (wt. %)	EDX results of the deposited film (wt. %)
Ti	90	88.7
Al	6	6.9
V	4	3.8

2.4 Electrical Characterization

Sheet resistance is considered as one of the most important parameters for an absorber layer.[36] The relation between resistance (R), resistivity (ρ), and sheet resistance (R_{sh}) are given in Equation 2.1.[37] The length (L), width (w), and thickness (t) parameters of the absorber layer are shown in Figure 2.8.

$$R = \rho \frac{L}{A} = \rho \frac{L}{wt} = \frac{\rho}{t} \frac{L}{w} = R_{sh} \frac{L}{w}$$

$$\rightarrow \boldsymbol{\rho = R_{sh}.t} \qquad \text{Equation 2.1}$$

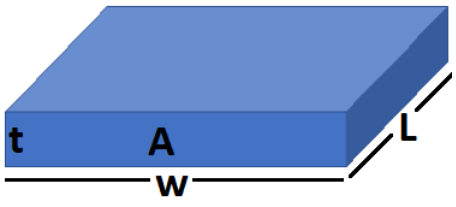

Figure 2.8. Dimensions of the thin film absorber layer.

It is known in the literature that reflection losses can be reduced, and broadband absorption can be achieved with the impedance matching, meaning that the sheet resistance of the absorber layer should match the characteristic free impedance of space (z), 377 ohm/sq.[38] Figure 2.9a shows an electromagnetic wave traveling in air that encounters the absorber layer. Here, the reflection from the first surface can be reduced by providing the same resistance as air. The equivalent circuit model is also given in Figure 2.9b.

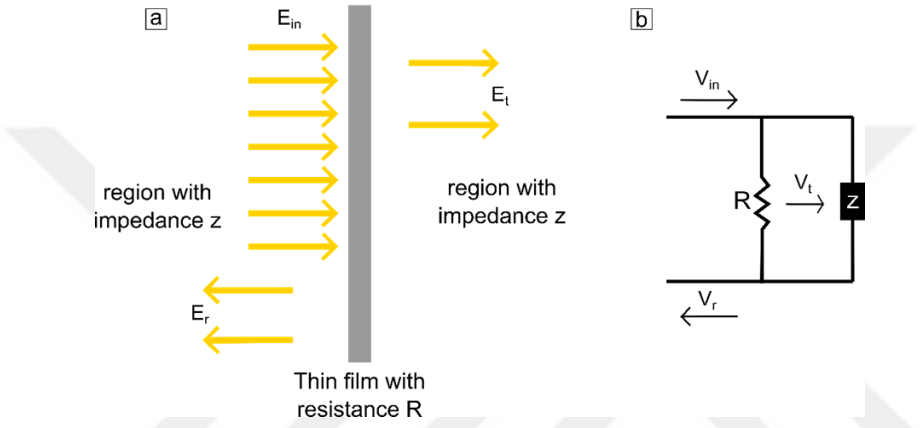

Figure 2.9. a) Schematic view of an electromagnetic wave encountering the absorber layer surface, and b) the equivalent circuit model.

Thus, after the thickness and deposition parameters are optimized, sheet resistance values are measured utilizing a 4-point probe station. Thin film absorber layers to be fabricated for sheet resistance measurements are prepared in a way that they could also be used in THz-TDS measurements. For this purpose, 8" Si wafer is coated with a passivation layer of Si_xN_y to isolate the metal absorber layer from the Si substrate with a dielectric medium using Plasma Enhanced Chemical Vapor Deposition (PECVD) technique. Thickness of the Si_xN_y layer deposited on the Si substrate is measured as 50 nm with Filmetrics optical profilometer. The Si/Si_xN_y wafer is then diced into square samples with a side length of 2.5 cm. After dicing, all the square samples are cleaned with Q-tip in an acetone bath and then in an isopropyl alcohol bath, rinsed and made ready for the deposition.

For each different thickness, 3 samples of Si/Si_xN_y are selected side by side, the middle sample is separated as a Si/Si_xN_y reference, and the other 2 samples are used for the TiAlV deposition. One of the TiAlV deposited sample is used for the sheet resistance measurement and the other one for the THz-TDS measurement. Sheet resistance values that are measured experimentally using a 4-point probe are given in Table 2.3. Considering Equation 2.1, since ρ is a constant being an intrinsic property of a material, sheet resistance will decrease with increasing thickness. Accordingly, a decreasing sheet resistance is observed experimentally as the TiAlV thin film thickness increased.

Table 2.3. Sheet resistance values of TiAlV films with different thicknesses.

Deposition duration (s)	*Thickness (nm)*	*Sheet Resistance (Ω/sq)*
75	7	470
106	10	290
160	15	165
213	20	127
320	30	78

Table 2.3 shows that the fabrication of a TiAlV absorber layer having a sheet resistance of 377 ohm/sq for impedance matching requires a thickness smaller than 10 nm. This thickness will not be enough to achieve a significant THz absorption to raise the absorber layer temperature. It is shown in Section 2.5 from a study of Naoki Oda [20] that when THz absorption of an absorber layer is plotted against the sheet resistance, the peak response is not achieved at 377 ohm/sq but observed at lower sheet resistance values corresponding to thicker absorber layers. It is previously mentioned while comparing 10 nm NiCr and 10 nm TiAlV layers that one can easily fabricate thicker layers of TiAlV without contributing much to the mass due to its low density.

Sheet resistances of TiAlV films are also measured after 2 days and 4 days to monitor the effect of surface oxidation. Sheet resistance values increased as a result of the natural oxide layer formation on the surface. For 75 seconds of TiAlV deposition the measured values are,

- 470 Ω/sq just after the deposition
- 570 Ω/sq 2 days later
- 580 Ω/sq 4 days later

Similarly, for 160 seconds of TiAlV deposition the measured values are,

- 165 Ω/sq just after the deposition
- 168 Ω/sq 2 days later
- 172 Ω/sq 4 days later

Sheet resistance values of the thick sample do not increase as dramatically as the thin sample. The value for 75 seconds of TiAlV deposition increased from 470 ohm/sq to 580 ohm/sq after 4 days showing a 23.4 % increase whereas the sheet resistance of 160 seconds of TiAlV deposition increased from 165 ohm/sq to 172 ohm/sq showing only a 4.2 % increase. The surface oxidation effect is more clearly observed in the thin sample, since the natural oxide layer thickness is more comparable with the overall film thickness for the thin sample compared to the thick one. This result highlights the importance of using a protection layer to prevent surface oxidation.

It is also possible to calculate sheet resistance values from THz frequency domain data. Figure 2.10 shows both the experimental sheet resistance values and the THz estimation of sheet resistance values. The most important achievement here is to show that it is possible to accurately estimate the sheet resistance values from noncontact THz optical measurements. Sheet resistance values are calculated using Equation 2.2 [39], where z_0 is characteristic free impedance of space, n is the refractive index of substrate, A_{ref} and A_{sample} are the amplitude values for Si/Si_xN_y and $Si/Si_xN_y/TiAlV$ samples obtained from their THz measurements respectively.

Details of THz measurements are given in Section 2.5. Here, I would only like to emphasize that these are noncontact measurements. Noncontact and thereby nondestructive nature of THz measurements can be the reason for it to easily replace the destructive probe measurements where the surface of the sample is damaged and contaminated.

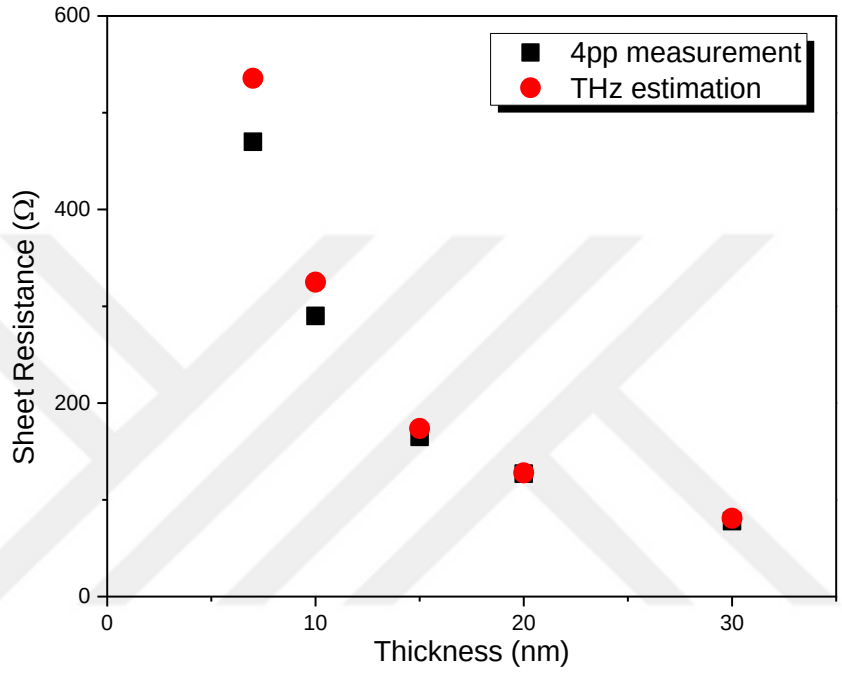

Figure 2.10. Experimental and THz estimated sheet resistance values for 7, 10, 15, 20, and 30 nm of TiAlV layer.

$$R_{sh} = \frac{z_0}{(n+1)\left(\frac{A_{ref}}{A_{sample}} - 1\right)} \qquad \text{Equation 2.2}$$

When thicker layers are fabricated, estimation seems to be more accurate. Figure 2.11 shows that the difference between experimental values and the THz estimations vanishes at thicker TiAlV layers. Sheet resistance values calculated from THz measurements for 7 nm and 10 nm seem to be overestimation. According to Equation 2.2, for estimating the sheet resistance R_{sh} to be higher, A_{sample} should be higher. This indicates that THz transmissions of thin samples are higher.

This might be due to the prominent effect of thickness nonuniformity for thinner layers. The thickness variation will result in regions both thinner and thicker than 7 nm throughout the sample, which will affect the overall THz transmission of 7 nm film more than the variations in a 250 nm thick film.

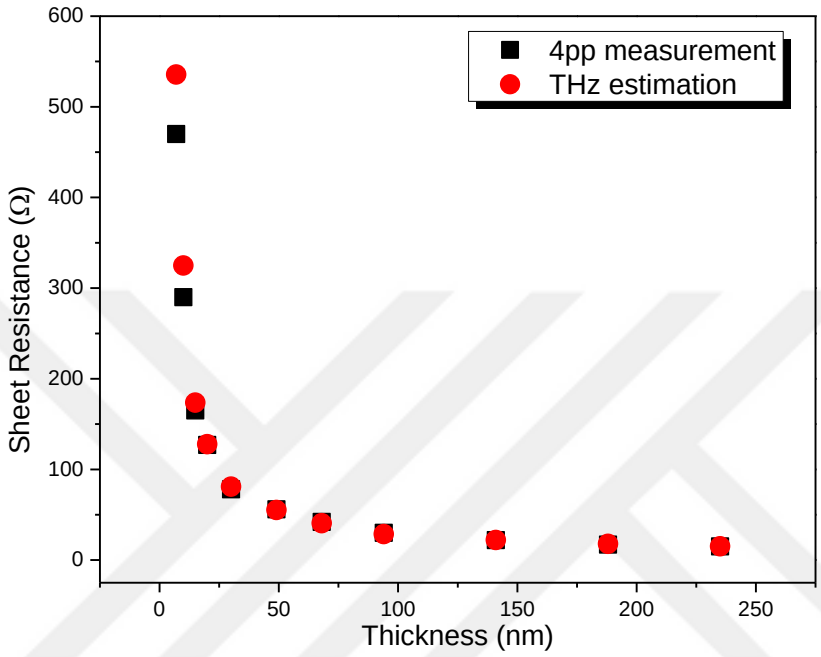

Figure 2.11. Experimental and THz estimated sheet resistance values for thicker TiAlV layers.

2.5 THz Optical Characterization

The THz-TDS setup used in this study is constructed by Yusuf Samet Aytekin in the Laser Spectroscopy Laboratory present in the Department of Chemistry, METU. The details about the system are explained thoroughly in the reference thesis.[40] To mention briefly, a low temperature grown GaAs (LT-GaAs) photoconductive array antenna with microlens array (BATOP, iPCA-21-05-1000-800-h) is used with a mode-locked Ti:Sapphire oscillator (Coherent Mantis, 80 MHz, 80 fs pulse width central wavelength: 800 nm) under an AC bias voltage of 15 V at 8 kHz in order to generate a THz signal.

The generated THz beam is collimated, focused to the sample, and collimated again using off-axis parabolic mirrors in 8F configuration in a humidity-free environment. Detection of the THz pulses is achieved by a combination of 500 µm ZnTe crystal (MTI Corporation), a quarter waveplate, Wollaston prism, and a balance photodiode.

A THz time domain signal is indeed a transient electric field. Figure 2.12 shows a typical THz time domain profile of a reference and a sample. Collected time domain data of all samples are interpreted according to their references. The reflection, absorption, and/or scattering caused by the sample will result in an attenuation of the incoming radiation, and the thickness and/or an index change will result in a delay of the THz pulse since the optical pathlength has changed. Hence, the decrease in the amplitude indicates a loss of the incoming radiation due to absorption/reflection of the sample whereas the right shift in the time domain is the delay of the incoming radiation and gives insight about the thickness/refractive index of the material.

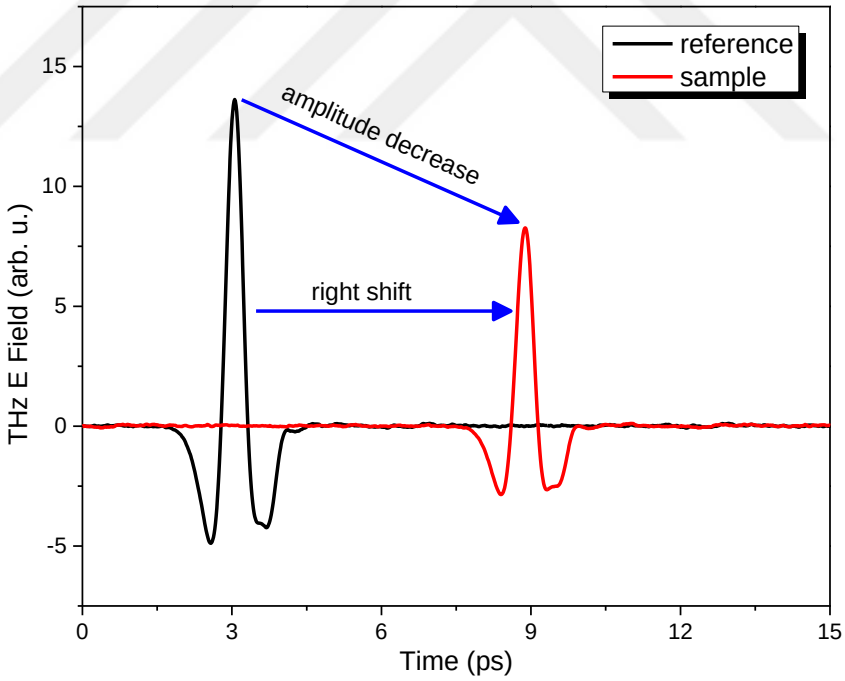

Figure 2.12. Time domain profiles obtained from a THz-TDS measurement.

Using only the delay (Δt) between the reference and sample in the time domain data, one can calculate the average index of a sample with thickness "d" using Equation 2.3 where c is speed of light.

$$n = 1 + \frac{c\Delta t}{d} \qquad \text{Equation 2.3}$$

Fast Fourier Transform (FFT) should be performed on the time domain data to obtain frequency domain properties. FFT provides frequency domain amplitude and phase information of THz pulses [41] which are shown in Figure 2.13 for the time domain data given in Figure 2.12.

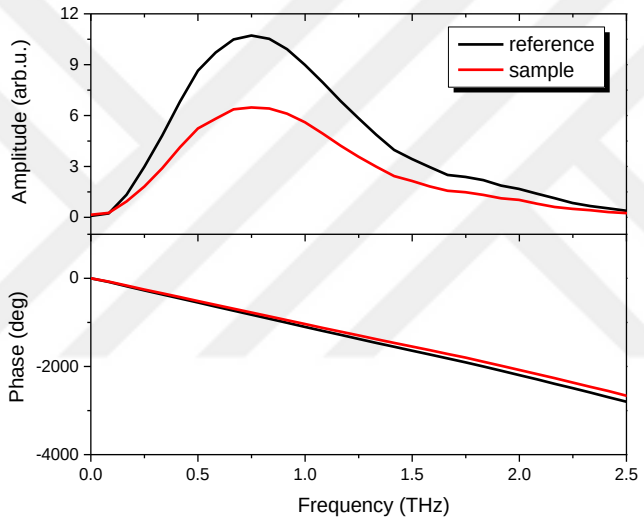

Figure 2.13. Frequency domain amplitude and phase data obtained by performing FFT on time domain data.

Using the frequency domain amplitude and phase data obtained from FFT, one can calculate transmittance (Equation 2.4), absorbance (Equation 2.5), absorption coefficient (Equation 2.6-2.7), n and k values (Equation 2.8-2.9), and so on.

$$T = \frac{P}{P_0} \qquad \text{Equation 2.4}$$

$$A = -\log T \qquad \text{Equation 2.5}$$

$$\alpha = -\frac{1}{d}\ln T \qquad \text{Equation 2.6}$$

In some resources, absorption coefficient is given as $\alpha = -\frac{2}{d}\ln T$, it is because the transmission is amplitude transmission and not power transmission there. Power is the square of amplitude, so it can be written as,

$$\alpha = -\frac{1}{d}\ln\frac{P}{P_0} = -\frac{1}{d}\ln\frac{A^2}{A_0^{\,2}} = -\frac{2}{d}\ln\frac{A}{A_0} \qquad \text{Equation 2.7}$$

$$n = 1 + \frac{c\Delta\varphi}{\omega d} \qquad \text{Equation 2.8}$$

$$k = \frac{c\alpha}{2\omega} \qquad \text{Equation 2.9}$$

Since water vapor has strong absorption characteristics at THz region, the THz beam path and the sample holder are in an atmosphere-controlled box. The percent relative humidity in the box is controlled, and measurements are started after 0% relative humidity is obtained with continuous purging. A reference Si/Si_xN_y is always measured before every Si/Si_xN_y/TiAlV sample. After all samples are measured, FFT is performed on their time domain data to obtain the characteristics in the frequency domain. Amplitude and phase information are obtained after performing FFT using common software such as excel or OriginLab and also TDS Spectrum Viewer.

Figure 2.14 shows the time domain profiles of the first set of samples. It is seen that the amplitude decreases as the thickness of the TiAlV layer increases from 7 nm to 30 nm. This amplitude loss indicates a decrease in THz transmission with increasing TiAlV thickness.

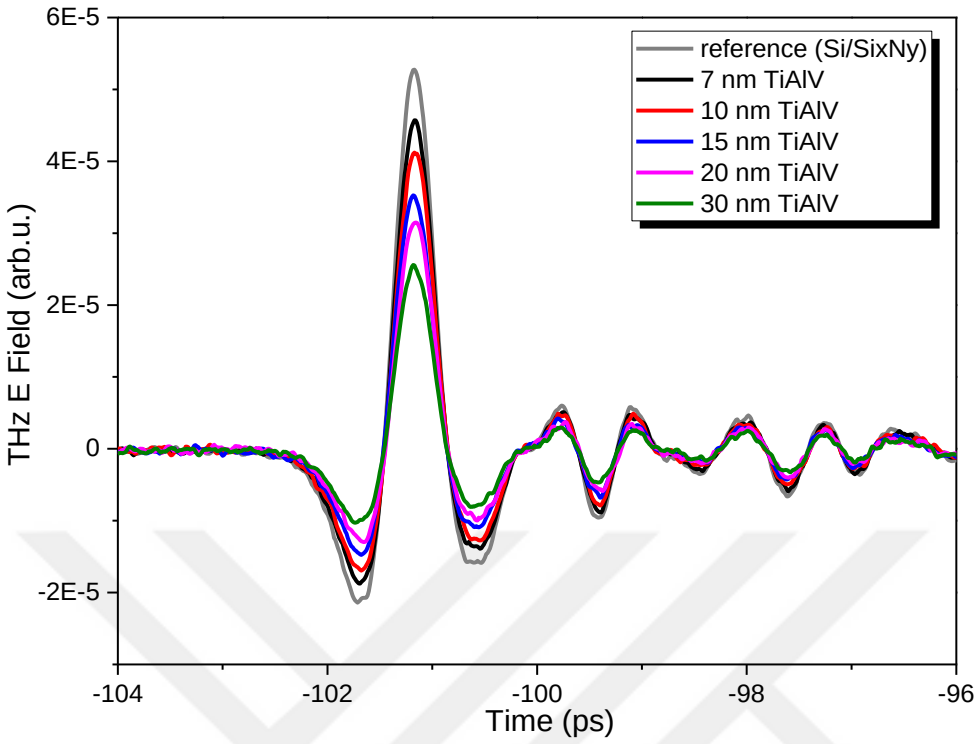

Figure 2.14. Time domain profiles of different thicknesses of TiAlV layers.

FFT is performed on the time domain data presented in Figure 2.14. Afterwards, experimental THz transmissions of TiAlV films having 7 nm, 10 nm, 15 nm, 20 nm, and 30 nm thicknesses are calculated using Equation 2.4. In Equation 2.4, P corresponds to the power obtained from FFT performed on the TiAlV sample, whereas P_0 is the power obtained from FFT performed on the Si/Si_xN_y reference, for all samples. THz transmission spectra in frequency domain are given in Figure 2.15 relative to the Si/Si_xN_y reference, corresponding to a value of 1. The decrease in THz transmissions shows the increase loss with increasing TiAlV thickness. This loss of incoming THz radiation is due to both absorption and reflection changes caused by the TiAlV layer itself. Unfortunately, as the thickness changes so does the resistance of the film and hence the reflection losses of the film.

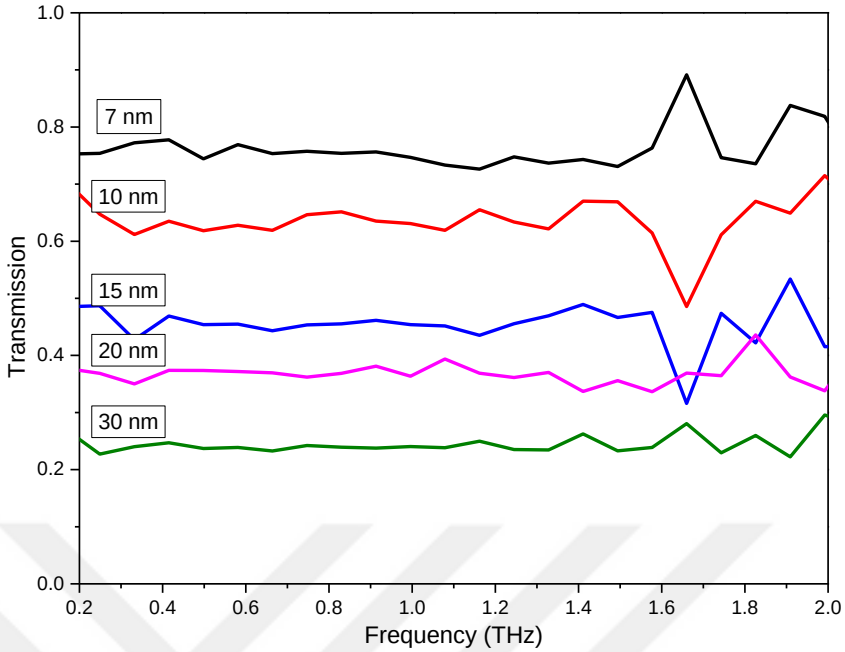

Figure 2.15. THz transmission profiles of TiAlV films having different thicknesses.

In a study by Naoki Oda [20], TiAlV absorber layer is used on top of a thermal isolation structure (TIS) for microbolometer applications. In that study, measured sheet resistance values are plotted against the total absorptance of TiAlV films which is given in Figure 2.16. The red rectangle on the graph in Figure 2.16 corresponds to the range of sheet resistances studied in this thesis. Here, it should be noted that peak THz absorption values are not at 377 ohm/sq but at lower sheet resistance values for all wavelengths in the reference paper. This is a significant result highlighting the fact that THz absorber layers do not require a sheet resistance of 377 ohm/sq for maximum absorption.

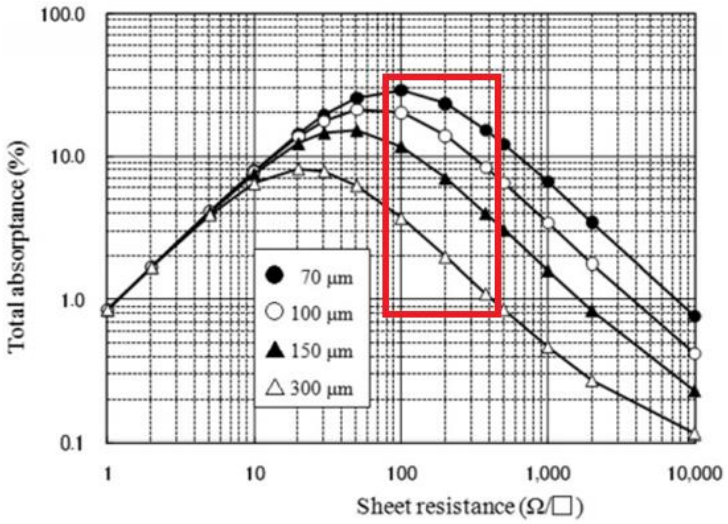

Figure 2.16. Total absorptance behavior as a function of sheet resistance of the THz absorber layer at different wavelengths.[20]

The total absorptance values of the films given in Figure 2.16 contains responses/losses of additional components such as air gaps in the TIS, the areal occupancy ratios etc., and they cannot be compared directly to the values calculated from THz measurements carried out in this thesis. However, since the authors changed only the absorber layer thickness and not any other parameter for the graph in Figure 2.16, the resulting profiles are caused by the differences in TiAlV thicknesses, as in our case. Differences in the total absorptance values relative to the sheet resistance depend only on the absorber film thickness. Therefore, the trends can be compared rather than exact values. For this purpose, the losses caused by TiAlV films are scaled accordingly to be in the same scale as total absorptance values at 1 THz reported in the reference paper. Scaled values from this thesis and actual values from the reference paper are plotted together in Figure 2.17 where the inset shows the zoomed-out graph. It is observed that scaled values (red squares) overlap one-to-one with values of the reference study at 1 THz (green dashed line).

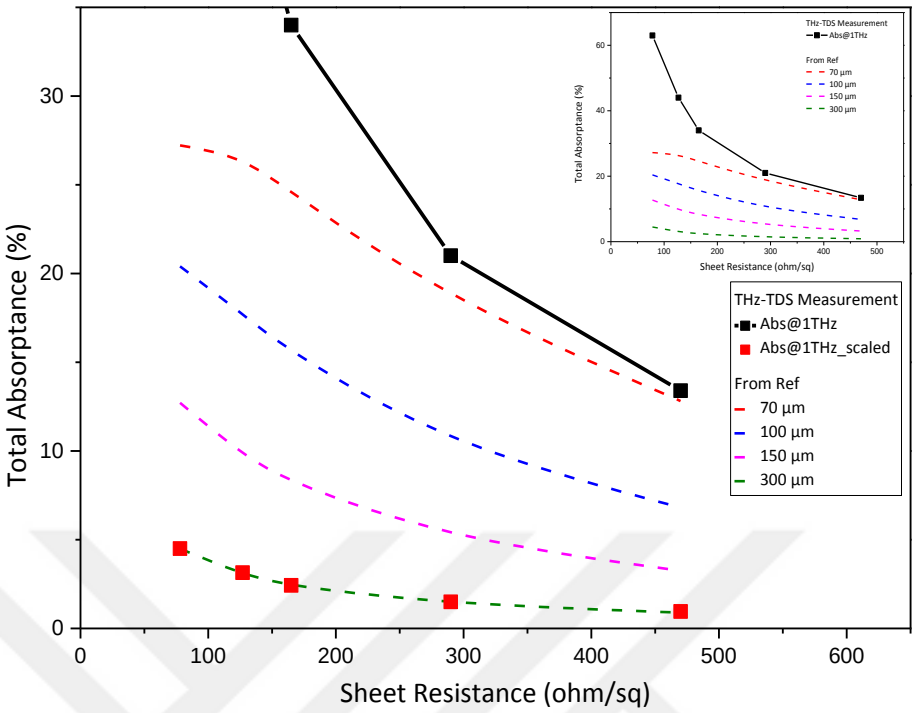

Figure 2.17. Comparison of the loss of incoming THz radiation at 300 µm (1 THz) from this thesis (red squares) and the total absorptance values at 1 THz from the reference paper (green dashed line). The result shows that the trends overlap very well.

The trend in this range indicates an increase in absorption with decreasing sheet resistance and thus increasing layer thickness. Considering this, one can increase the layer thickness and consequently the mass for an enhanced absorption. Equation 2.10 gives the formula for calculating the time constant, τ, which emphasizes the negative effect of increasing the mass.[42]

$$\tau = \frac{C_{th}}{G_{th}} \qquad \text{Equation 2.10}$$

Here, C_{th} is the thermal capacitance or thermal mass and G_{th} is the thermal conductance.

A microbolometer is constantly open to the incoming electromagnetic radiation, and it responds to temperature changes within the duration of its time constant which can be considered as the response time.

Since, time constant is a critical parameter which defines the speed of the detector, there are studies focusing on reducing the thermal mass for lowering the time constant.[43, 44] The lower the time constant the faster is the detector. Increasing the thickness of the absorber will increase the absorption until a certain point but will also increase the mass which will result in a higher time constant, and thus a slower detector response. Therefore, one should decide on the absorber layer thickness by considering both its positive effect on the absorption and its negative effect on the mass and thereby the time constant.

In addition, the loss of incoming THz radiation in this study is the sum of reflection and absorption of the TiAlV film. Therefore, knowing the contribution of the reflection will enable to calculate the absorption of the THz radiation. Unfortunately, there is no setup of reflective measurements, thus the reflection losses need to be estimated. One of the approaches is the use of refractive index of the film to use it in the Fresnel equation to estimate the reflection losses. However, due to a very thin film thickness in nm size and varying thickness of Si/Si_xN_y reference possibly greater than the film thickness, a positive phase difference could not be observed after performing FFT especially for the thin TiAlV layers. Thus, the calculated refractive index values were not meaningful. Therefore, as a second approach, reflection coefficients are calculated by using Equation 2.11 where z_{in} is the measured sheet resistance values and z_0 is the characteristic impedance of free space.[36] Once the reflection coefficients are obtained, they are used to calculate the absorbed power using Equation 2.12.[36] However, this is only true for microbolometer structures having mirror layers that prevent transmission losses and provide perfect reflection. As mentioned earlier, there are reflection, absorption, and transmission losses in our case. Therefore, using Equation 2.12, the loss caused by only the reflection is calculated and eliminated. The reflection corrected values are presented in the column named “Estimated Transmission after Reflection Loss” in Table 2.4.

$$\Gamma = \frac{Z_{in} - Z_0}{Z_{in} + Z_0} \qquad \text{Equation 2.11}$$

$$P_{abs} = (1 - |\Gamma|^2) P_{in} \qquad \text{Equation 2.12}$$

The next column in Table 2.4 is the "Measured Transmission" column which gives the experimentally measured THz transmission values using the THz-TDS setup. By taking the difference of these two columns, one can see the effect of absorption with increasing layer thickness.

Table 2.2 presents all the parameters that are measured and calculated for TiAlV layers including deposition times, thicknesses, sheet resistances, THz transmissions and resulting absorptions at 0.8 THz. Results show an increase in THz absorption with the increase in thickness or decrease in sheet resistance until a certain point, as expected. However, it is noticed that the absorption per unit thickness does change after a certain thickness of TiAlV. Absorption per unit thickness decreases with increasing thickness especially after the coating time of 520 seconds. Thus, fabricating a thicker absorber becomes disadvantageous after a point where it only increases the mass in a microbolometer structure and does not contribute much to the absorbance of the film, as mentioned earlier in the discussion of the time constant.

Part of the results here are presented at the 9th International Workshop on Terahertz Technology and Applications in 2020, at Fraunhofer ITWM, Germany. Part of the results will also be presented at IRMMW-THz 2022, that will be held in Delft, The Netherlands.

Table 2.4. Transmission and absorption values for TiAlV layers with different thicknesses.

Coating Time (s)	Thickness (nm)	Sheet Resistance (ohm/sq)	Estimated Transmission after Reflection Loss	Measured Transmission	Difference (Estimated Absorption)	Difference (Estimated Absorption) per unit thickness (nm^{-1})
75	7	470	0.988	0.754	0.234	**0.0334**
106	10	290	0.983	0.651	0.332	**0.0332**
160	15	165	0.847	0.455	0.392	**0.0261**
213	20	127	0.754	0.369	0.385	**0.0193**
320	30	78	0.568	0.239	0.329	**0.0110**
520	49	56	0.450	0.152	0.298	0.0061
720	68	42	0.361	0.108	0.253	0.0037
1000	94	30	0.273	0.069	0.204	0.0022
1500	141	22	0.208	0.044	0.164	0.0012
2000	188	17	0.165	0.028	0.137	0.0007
2500	235	15	0.147	0.024	0.123	0.0005

CHAPTER 3

ACTIVE MATERIAL

3.1 Material of Choice, WO_3-V_xO_y

WO_3-V_xO_y is evaluated as the candidate active material layer for THz microbolometers. Active material is also called the "detector element", "thermosensitive", or "temperature sensitive" material in different resources which all mean a material that is capable of sensing a temperature change. Electromagnetic radiation absorbed by the detector heats up the pixel and increases its temperature. This temperature increase is "sensed" by the active material by changing its resistance, and the resultant resistance change is read by readout electronics. As mentioned earlier, the absorption of THz radiation will not increase the temperature as much as the more energetic Infrared waves, and that is why it is essential for a THz microbolometer to have a remarkable resistance change even with a very small change in the temperature. Thus, a high TCR is a critical parameter to achieve high sensitivity THz microbolometers while considering its negative effect on the noise.

A variety of materials have been studied as active materials in the literature. Most widely used commercial active material is V_xO_y, followed by amorphous Si and SiGe.[14, 45-48] METU MEMS Center has developed optimized recipes for different active materials in past years, and has been using V_xO_y recently. In a study by Başak Kebapçı [49], TCR values of -0.74 %/K and -0.8 %/K has been achieved for two different V_xO_y samples fabricated using different deposition approaches, and these values are significantly increased with annealing to -1.6 %/K and -4.35 %/K. However, it is stated that resistance values were not reliable and there was an enhanced noise due to residual V_xO_y contaminations remained on electrodes because the active material was being patterned using wet etching.

Another study by Özgecan Dervişoğlu on using $V_2O_5.nH_2O$ active material which is fabricated by sol-gel technique showed a TCR value around -2 %/K.[50] Finally, the study of Numan Eroğlu showed that the use of V-W co-sputtering as in the present thesis study results in TCR value of -3.31 %/K for the sample having 113 ohm.cm resistivity value which is higher than the highest resistivity presented here, and noise corner frequency of 0.9 kHz.[51] In that study, active material layers were patterned again by using wet etching as in [49]. In the present study, active material layers are patterned by lift-off process to eliminate possible residual V_xO_y, undercut, and thus reproducibility problems. All these previous studies focused on IR microbolometer applications. Now, the present thesis study and the corresponding reference paper [52] is the first study conducted at METU MEMS Center considering THz microbolometer applications and investigating the mixed phase V_xO_y active material in THz region utilizing THz-TDS.

Indeed, V_xO_y had been utilized as the detector element for microbolometers since 1980s first by Honeywell Sensor and System Development Center under classified projects for US military until it had been announced and patented in 1992 [53, 54]. Among all active material candidates, V_xO_y dominates the industry due to its high TCR and low electrical noise properties. Here it should be noted that there is a trade-off between high TCR and low noise. High TCR value brings a high resistivity value with itself.[55] If a vanadium oxide phase having a high TCR, i.e.V_2O_5 is utilized as the active material itself, resistivity would be too high exceeding the limits of Complementary Metal-Oxide Semiconductor (CMOS) circuits on which MEMS-based microbolometers are fabricated. This high resistivity would bring undesired electrical noise.[56] An active material should thus have a high TCR with a resistivity within the limits of CMOS circuitry being in the optimized resistivity range and not too high to introduce enhanced noise. Since vanadium is capable of forming various oxide phases with each having different resistivity and TCR values, one can tune the resistivity and TCR by adjusting the phases in proper amounts. Having a control on concentrations of individual vanadium oxide phases is essential for reproducible and optimized active materials.

In this thesis, such phase ratio control for the adjustment of CMOS-compatible resistivity while maintaining a high TCR is shown to be possible with V-W reactive co-sputtering. The active material is thus chosen as WO_3-V_xO_y to study the control on the resistivity and TCR values of V_xO_y films by adjusting the phase concentrations through V-W reactive co-sputtering. Details of noise measurements performed on pixel structures that contain the same active material are given in the reference thesis.[57]

3.2 Fabrication and Thickness Measurements

In the fabrication of active material layers, the process flow should be designed by taking the thermal budget for the MEMS-above-CMOS integration into consider. High-temperature processes are not compatible with CMOS readout circuits on which microbolometers are monolithically integrated utilizing surface micromachining techniques.[58] Therefore, in this study all the active material layer fabrications are performed at room temperature without any in-situ/post annealing steps. The V_xO_y and WO_3-V_xO_y thin films are deposited on quartz substrates by V-W reactive DC magnetron co-sputtering at room temperature. The schematic demonstration of the fabrication is given in Figure 3.1.

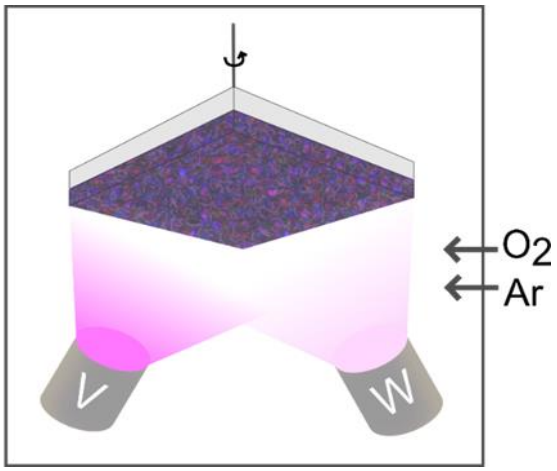

Figure 3.1. Reactive co-sputtering of V and W in O_2/Ar environment.

Quartz substrate is preferred over Si/Si_xN_y in this case, since it showed no difference in its THz profile at higher temperatures and became an ideal reference for measurements including heating which are shown in Section 3.5 in detail.

Commercial V target (K.J. Lesker, 99.8%) and W target (K.J. Lesker, 99.95%) both having 4" of diameter are co-sputtered in a sputtering chamber (AJA INTERNATIONAL, Inc.) different than the chamber that TiAlV depositions are performed in. The reason for using a different chamber is that V_xO_y or WO_3-V_xO_y depositions utilize reactive sputtering in high purity Oxygen and Argon environment with a ratio of 12% Oxygen. Since target materials would be exposed to oxygen during reactive sputtering, the corresponding chamber should be dedicated to reactive sputtering of desired targets, together with inert target materials if obligatory.

W target is not used for the V_xO_y sample meaning that W sputtering power is 0 Watt for V_xO_y sample. For V-W co-sputtered samples, the sputtering power of W target is increased from 40 Watt to 50 Watt. Increasing the W sputtering power will increase the number of atoms eroded from the target surface and will result in a higher W concentration.

V_xO_y and WO_3-V_xO_y films are deposited using the same conditions i.e., same gas flows with oxygen ratio of 12% and same sputtering time of 1300 seconds except the W sputtering power. W sputtering power is the only parameter changed in between the samples, and it is adjusted as 0 Watt for the V_xO_y sample, 40 Watt, and 50 Watt for the two V-W co-sputtered samples.

Deposited film thicknesses are measured from cross-section images that are given in Figure 3.2 using SEM (Hitachi). Thicknesses are measured as 248 nm, 321 nm, and 323 nm for the V_xO_y sample, first WO_3-V_xO_y sample with W sputtering power of 40 Watt, and the second WO_3-V_xO_y sample with W sputtering power of 50 Watt, respectively.

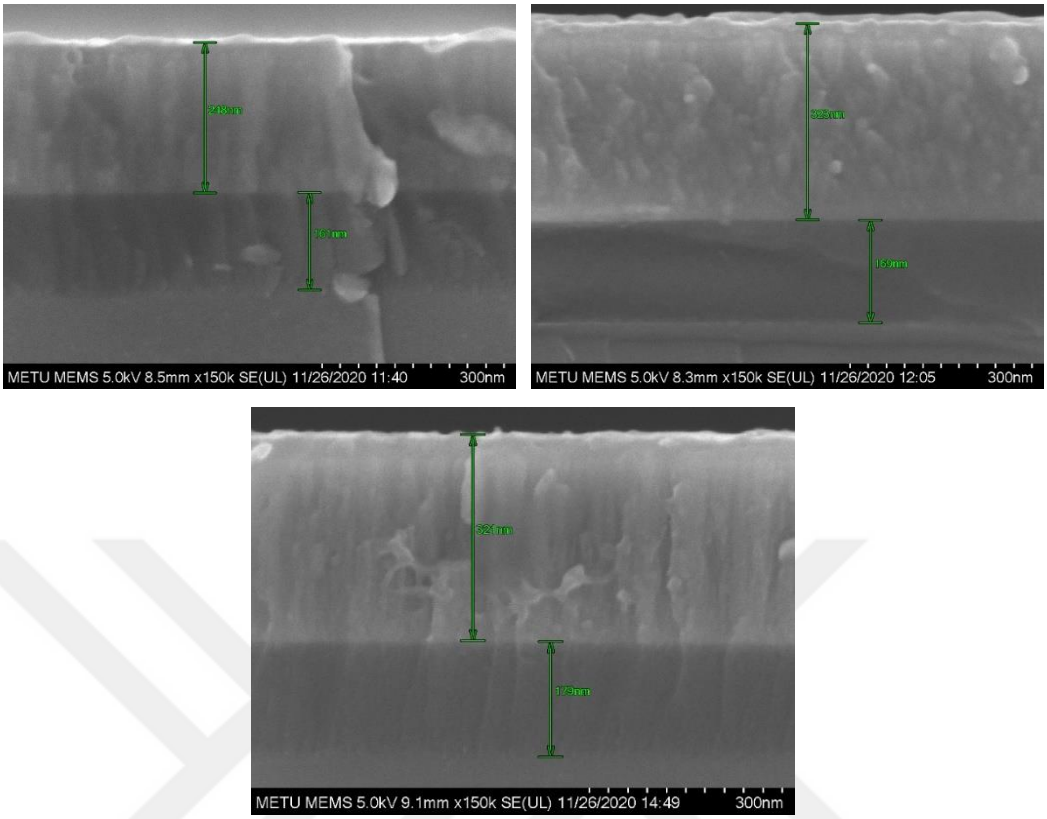

Figure 3.2. Cross-section SEM images of a) V_xO_y, b) WO_3-V_xO_y with 40 Watt, and c) 50 Watt of W sputtering power.

3.3 **Structural Characterization-X Ray Photoelectron Spectroscopy (XPS)**

Structural characterizations of V_xO_y and WO_3-V_xO_y thin films utilizing XPS are performed using ThermoFisher Scientific K-alpha X-Ray Photoelectron Spectrometer in Bilkent UNAM Facility with a monochromated X-ray source of Al-Kα and with an energy step of 0.158 eV. Literature studies suggest that Ar^+ ion etching could result in preferential etching of oxygen and change the original film composition [59-61]; therefore, the data presented here are from the surface of films that are collected without any etching process. C1s peak of adventitious carbon is used as the energy reference for the calibration of binding energies.[61, 62]

The concentration of each individual element (W, V, and O) is found by dividing its normalized peak area (NPA) to the sum of normalized peak areas of all the elements using Equation 3.1.

For instance, W concentration is calculated as,

$$W_{NPA} = \frac{W_{NPA}}{W_{NPA} + V_{NPA} + O_{NPA}} \qquad \text{Equation 3.1}$$

where W_{NPA} is the sum of $W4f_{5/2}$ and $W4f_{7/2}$ normalized peak areas. NPA is calculated for each element by dividing its peak area to several constants using Equation 3.2,

$$NPA = \frac{\text{Peak Area}}{SF \times TXFN \times ECF} \qquad \text{Equation 3.2}$$

where SF, TFNX, and ECF stand for the sensitivity factor, transmission function, and energy compensation factor, respectively. The instrument provides transmission function and energy compensation factor values, whereas each energy state has its own sensitivity factor and various sensitivity factors are reported in the literature for $V2p_{3/2}$, W4f, and O1s core energy states. Here, the Scofield sensitivity factors of 6.118, 11.059, and 2.881 are used for $V2p_{3/2}$, W4f, and O1s core energy states respectively, which are obtained from the database of the device provider.

W concentrations of V_xO_y films are determined from W4f core energy states given in Figure 3.3. The spectrum of the V_xO_y sample (Figure 3.3, top panel) does not include any W4f energy state, as expected. The broad peak appearing in the high binding energy side of the spectrum originates from the V3p energy state. This broad peak around 42 eV is common in all samples and has no relation to W.[63, 64] After V-W co-sputtering takes place, two peaks appear at 37.17 eV and 35.05 eV which correspond to $W4f_{5/2}$ and $W4f_{7/2}$ states, respectively. It is observed that their intensities increase with the increase in W sputtering power, as expected. Furthermore, these binding energies correspond to W^{6+} oxidation state, indicating the presence of WO_3.[62]

W concentrations for these two co-sputtered samples are calculated by placing the sum of $W4f_{5/2}$ and $W4f_{7/2}$ normalized peak areas in the numerator in Equation 3.1, and found as 5.6% and 7.2%, respectively.

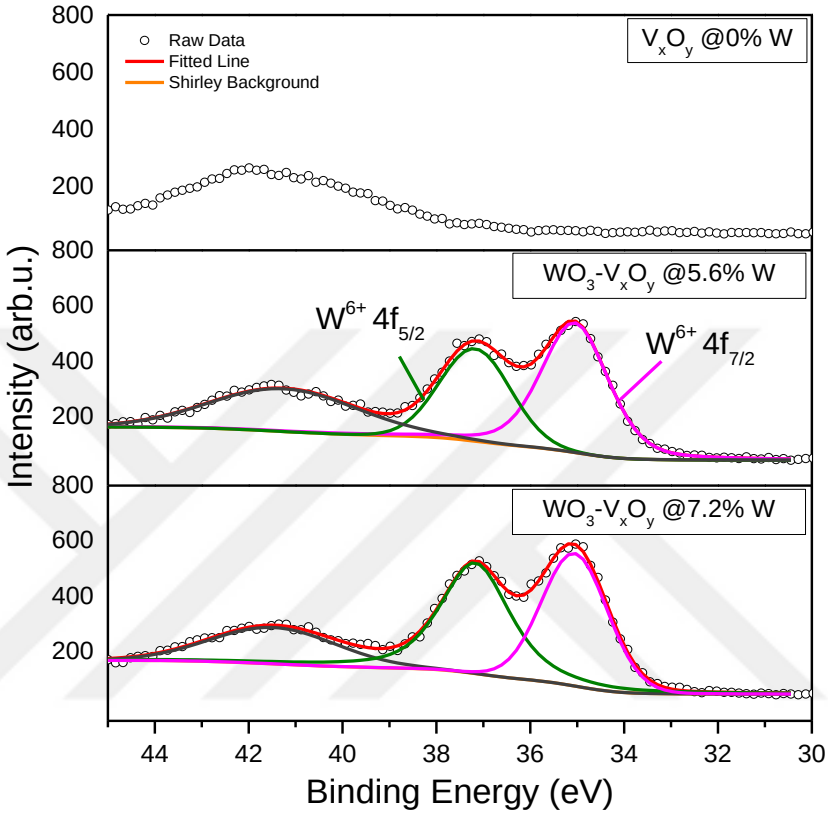

Figure 3.3. High resolution $W4f_{5/2}$ and $W4f_{7/2}$ spectra of V_xO_y and WO_3-V_xO_y films.

Figure 3.4 shows high resolution $V2p_{3/2}$ spectra of V_xO_y and WO_3-V_xO_y films. Deconvolution of $V2p_{3/2}$ spectra reveals the presence of V_6O_{13} and V_4O_9 phases, which are common in all V_xO_y and WO_3-V_xO_y samples. These phases correspond to a valence state between V^{4+} and V^{5+}. After V-W co-sputtering, a new phase, V_2O_5 (V^{5+}), emerges in the spectra of these two WO_3-V_xO_y films (Figure 3.4, mid and lower panels).

In the $V2p_{3/2}$ spectrum of the V_xO_y film, two peaks for V_6O_{13} and V_4O_9 phases are located at 516.6 eV and 516.2 eV (Figure 3.4, top panel).

The fittings result in FWHM values of 2.2 eV and 3.3 eV for V_4O_9 and V_6O_{13} phases, respectively. These values are consistent with previously reported values in the literature.[60, 65]

Relative concentrations of these phases are calculated again by using Equation 3.1 as 62.7% and 37.3%, and they decrease with V-W co-sputtering while the V_2O_5 phase appears as a new phase in the spectra of these WO_3-V_xO_y films. The $V2p_{3/2}$ spectrum of the WO_3-V_xO_y film having 5.6% W concentration is deconvoluted into three peaks located at 517.0 eV, 516.5 eV, and 516.3 eV which are corresponding to V_2O_5, V_4O_9, and V_6O_{13} phases with relative concentrations of 22.5%, 53.7%, and 23.8%, respectively.[65, 66] Calculations from the $V2p_{3/2}$ spectrum of the WO_3-V_xO_y film having 7.2% W concentration indicate that the relative concentration of V_2O_5 phase increases even to 38.0%, and those of V_4O_9 and V_6O_{13} phases decrease to 40.7% and 21.3%, respectively.

Table 3.1 summarizes peak deconvolution parameters of fitted peaks, and relative phase concentrations calculated from normalized peak areas using Equation 3.1.

In short, W4f spectra show the lack of W in the V_xO_y sample and that the amount of W increases from the V_xO_y sample to the V-W co-sputtered samples as the sputtering power for W increases, as expected. With V-W reactive co-sputtering, a new vanadium oxide phase, V_2O_5, is also formed together with WO_3 and its concentration increases with increasing W sputtering power and thus W concentration.

Considering that the V_2O_5 phase is a high TCR phase, results are very promising. It shows that it is possible to form and increase the concentration of this high TCR phase by only changing the sputtering power of W with a controlled V-W reactive co-sputtering. The possibility of a controlled amount of V_2O_5 phase formation in the V_xO_y films is a favored situation and would be highly valuable for the fabrication of high TCR films for THz microbolometers.

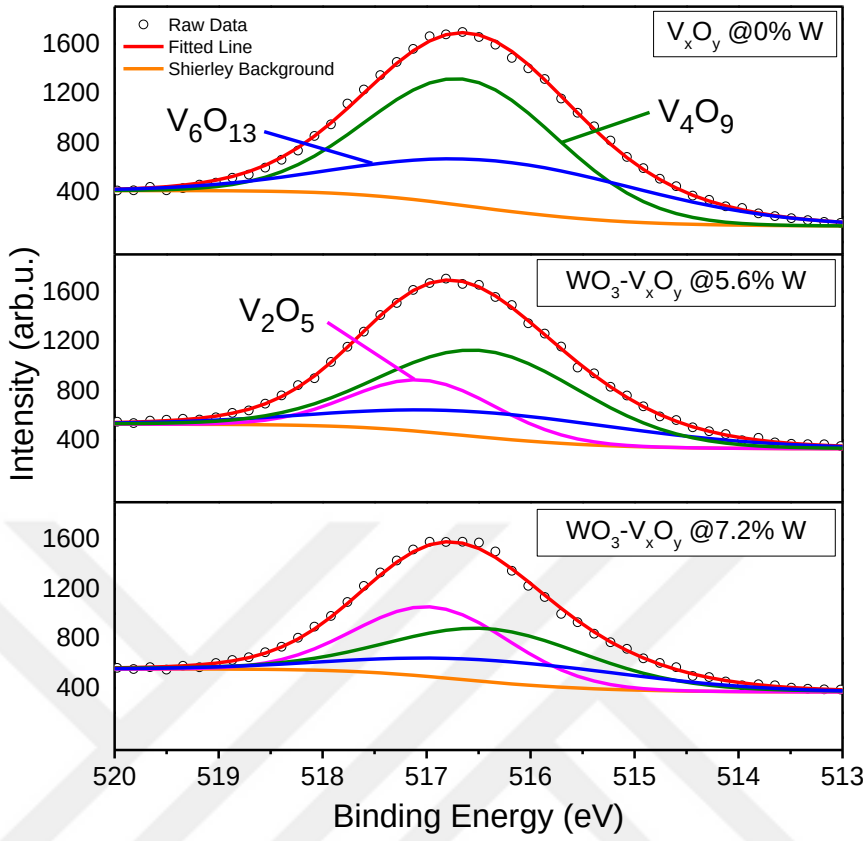

Figure 3.4. High resolution V2p$_{3/2}$ spectra of V_xO_y and WO_3-V_xO_y films.

Table 3.1. Peak deconvolution parameters and phase concentrations of V_xO_y and WO_3-V_xO_y films.

Sample	BE (eV)	FWHM (eV)	Phase	Phase Concent. (%)	W Concen (%)
S0	516.64	2.15	V_4O_9	62.7	0
	516.2	3.3	V_6O_{13}	37.3	
S1	517.03	1.63	V_2O_5	22.5	5.6
	516.47	2.27	V_4O_9	53.7	
	516.29	3.37	V_6O_{13}	23.8	
S2	516.94	1.74	V_2O_5	38.0	7.2
	516.38	2.25	V_4O_9	40.7	
	516.2	3.1	V_6O_{13}	21.3	

3.4 Electrical Characterization

V_xO_y and WO_3-V_xO_y films are deposited on sandwich-type electrodes for electrical characterizations. Electrical resistances are then measured using a 2-point probe station. The cross-section view of the sandwich-type electrode and the 2-point probe resistance measurement is shown in Figure 3.5.

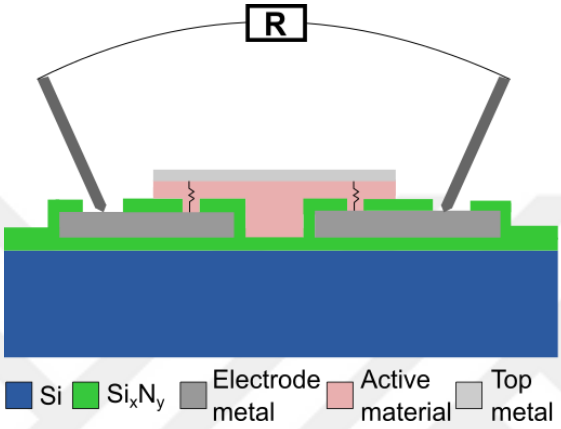

Figure 3.5. Cross-sectional view of a sandwich-type electrode with 2-point probe for a resistance measurement.

These sandwich-type electrodes are being prepared in METU MEMS Center for testing active material properties periodically. Required process steps are given in

Figure 3.6. In this process flow, the electrode metal NiCr is protected by Ti hard mask during NiCr patterning. However, it is observed that removing the Ti hard mask in the following steps is challenging most probably due to the adhesive nature of Ti. In the literature, the study by Li *et al.* proposes that a TiNiCr alloy may form in between Ti and NiCr.[67] Figure 3.7a shows the clear boundary between NiCr and photoresist (PR). When Ti is deposited on NiCr, there is no clear boundary observed between NiCr and Ti as can be seen in Figure 3.7b. Authors claim that there might be a TiNiCr alloy formation in the interface due to the strong adhesive nature of both Ti and NiCr.

Therefore, a new process flow is designed by eliminating the Ti hard mask deposition in this thesis study. In the new process flow, the top SiN layer which was being deposited after Ti hard mask removal is used as the hard mask itself.

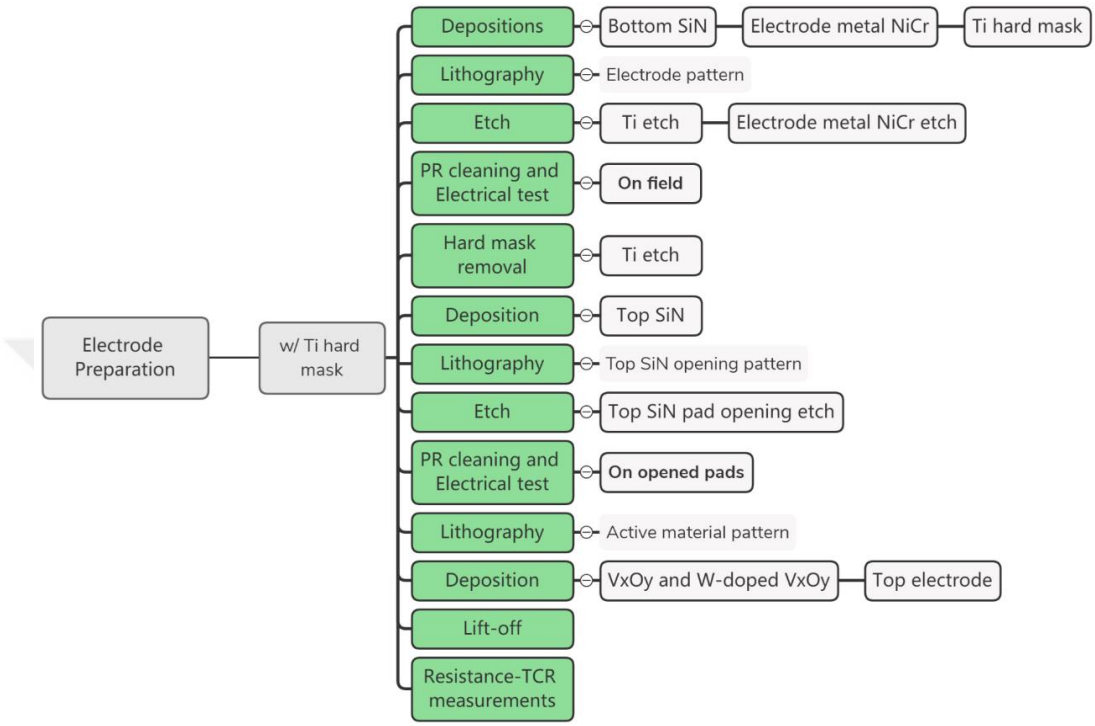

Figure 3.6. Electrode structure process flow by using Ti as a hard mask for protecting NiCr.

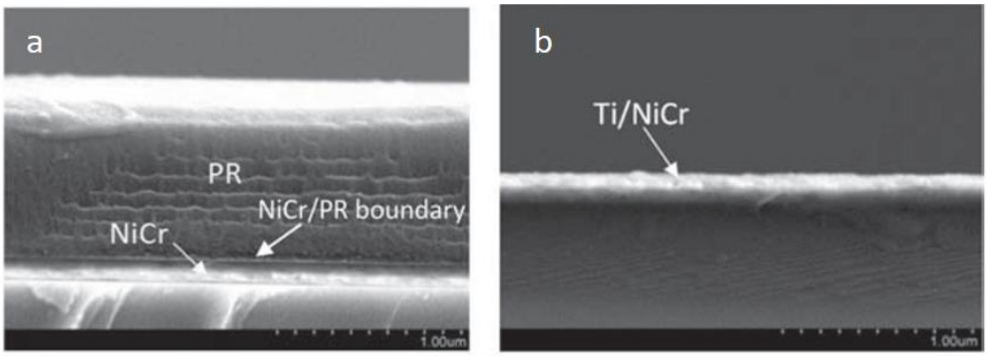

Figure 3.7. a) The clear boundary between PR/NiCr and b) no boundary between Ti/NiCr indicating a TiNiCr alloy, in the study by Li *et al.* [67]

The proposed process flow is given in Figure 3.8 in which red steps are removed from the old process flow, and blue steps are added to the process flow given in

Figure 3.6. Removing Ti hard mask and using the top SiN layer as a hard mask reduces the number of steps and improves the process as SiN does not form an alloy with NiCr. SiN becomes a preferable choice by serving as an inert hard mask.

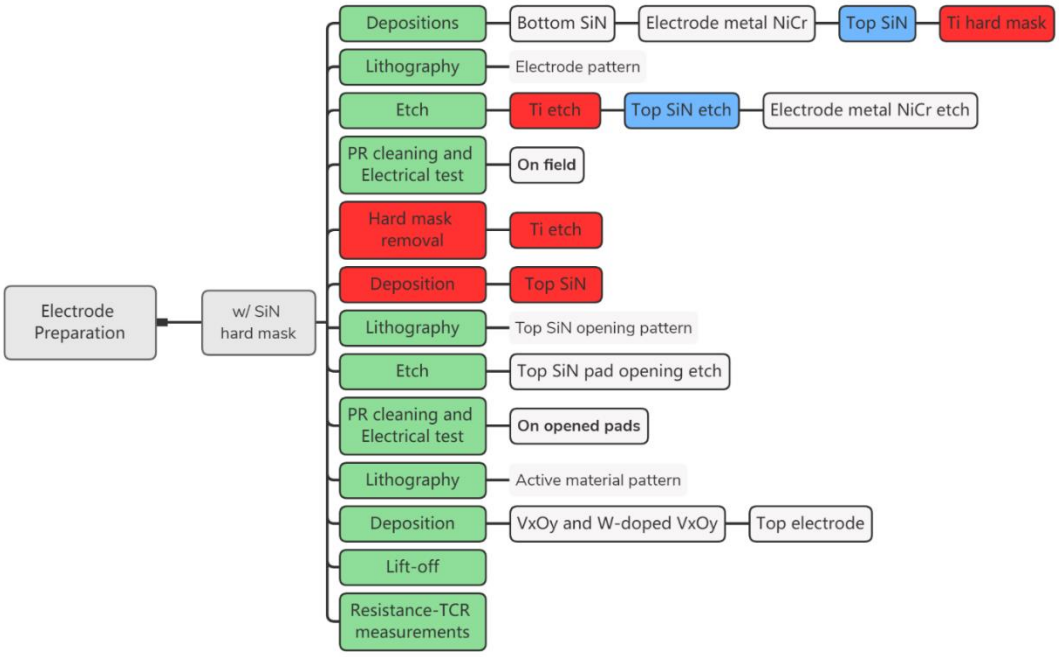

Figure 3.8. Proposed process flow by using top SiN as the hard mask for protecting NiCr.

These sandwich-type electrode structures are fabricated on an 8" Si wafer using the proposed process flow with SiN as hard mask, and schematic cross-section views after each step are given in Figure 3.9.

Figure 3.9a shows first depositions starting with a bottom passivation layer of Si_xN_y using PECVD. The electrode metal e.g., NiCr is then deposited using DC magnetron sputtering, and finally top Si_xN_y is deposited again using PECVD. On top of these layers, a photoresist is spin coated as the first step of the first lithography using the electrode mask (Figure 3.9b) and it is patterned after UV exposure and developing (Figure 3.9c).

The patterned photoresist protects the desired parts of top Si_xN_y and NiCr. The unprotected parts of the top Si_xN_y layer are dry etched using reactive ion etching (Figure 3.9d) followed by NiCr dry etch again by using reactive ion etching (Figure 3.9e). The remaining photoresist is then cleaned completely in a commercial photoresist strip solution (Figure 3.9f). Second lithography is performed to create openings on the top Si_xN_y layer with a pad opening mask (Figure 3.9g). The Si_xN_y is removed from the openings again by reactive ion etching (Figure 3.9h) followed by cleaning the wafer in a photoresist strip solution. The last lithography for the deposition of active material is performed with a lift-off photoresist (Figure 3.9i) on which the active material and the top electrode are deposited by DC magnetron sputtering (Figure 3.9j). The wafer is then soaked in acetone to remove the lift-off photoresist together with the active material and top metal deposited on it (Figure 3.9k). The active material is finally patterned and placed on electrodes, and resistance measurements are performed using probes on opened NiCr pads as shown in Figure 3.5.

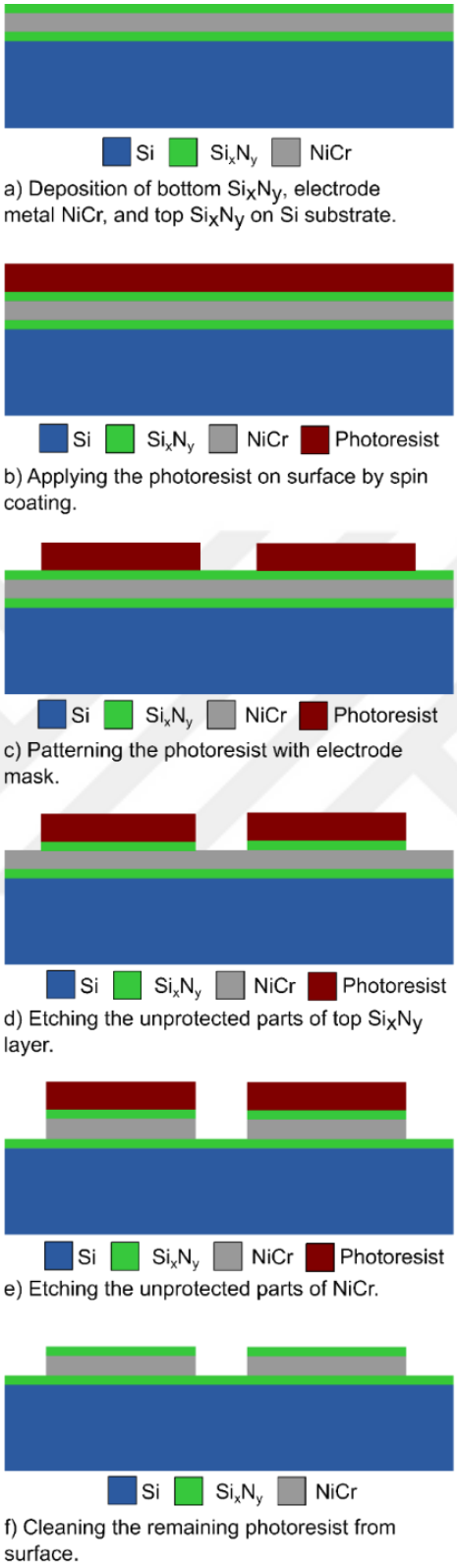

Figure 3.9. Process flow for a sandwich-type electrode.

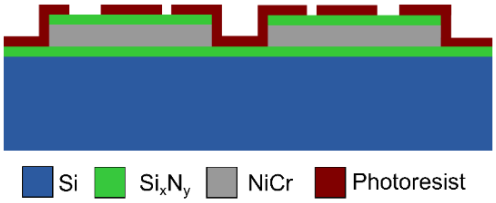

g) Applying the photoresist by spin coating and patterning it with pad opening mask.

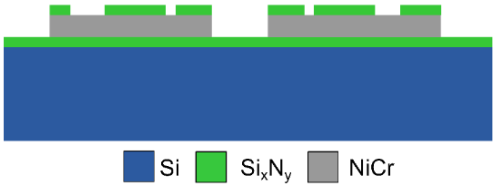

h) Etching the top Si_XN_Y to form openings and cleaning the remaining photoresist.

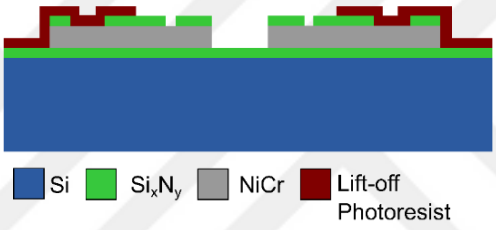

i) Applying the lift-off photoresist and patterning it with active material mask.

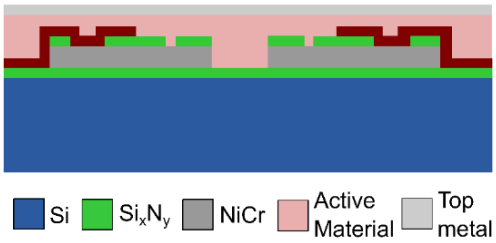

j) Deposition of the active material and the top electrode.

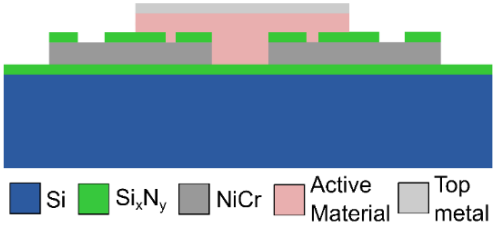

k) Patterning the active material and top electrode by lift-off.

Figure 3.9 (continued). Process flow for a sandwich-type electrode.

WO_3-V_xO_y depositions are being performed on these electrodes periodically at METU MEMS Center. Figure 3.10 highlights the reproducibility of the active material with the desired resistance value by showing the resistance measurements of four different depositions. The number of data points are different because these four different samples have different number of electrode patterns on them to be measured.

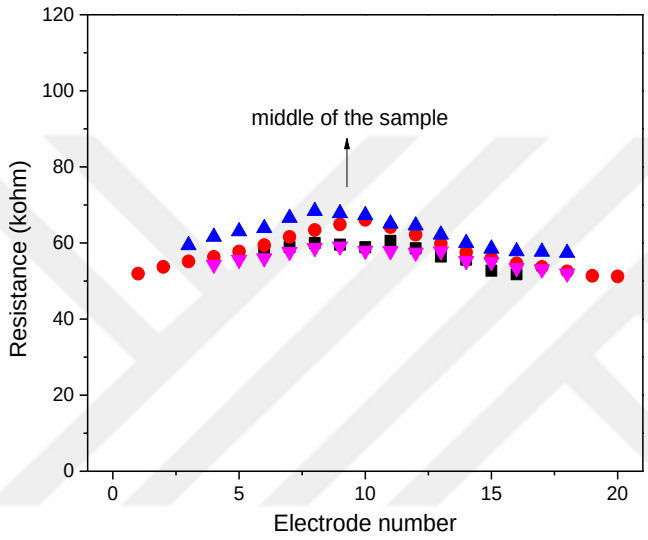

Figure 3.10. Resistance uniformity of four different samples having different number of electrode structures on them.

Resistance values are lower at edges, and they increase slightly in the middle of the sample. This is because the reactive ion etching starts from the outer edge of the wafer and then continues to the middle, making Si_xN_y openings larger at the edges. When the Si_xN_y opening areas are larger (larger A), resistance decreases according to Equation 3.3.

$$R = \rho \frac{L}{A} \qquad \text{Equation 3.3}$$

Since resistance is a geometry-dependent parameter and resistivity is an intrinsic property of a material, all the resistance values are converted to resistivities using the relationship in Equation 3.3.

Electrical characterizations are also performed as a function of temperature, for this purpose, samples are heated utilizing a TEC placed on the probe station. Figure 3.11 shows the TCR measurement setup where HP 34401a multimeter is connected to probes and used to read resistance values while changing the temperature of the TEC underneath. Agilent E3631A power supply is used to apply voltage to the TEC to change its temperature. TEC is also connected to a handheld Agilent U1272A multimeter to monitor the temperature.

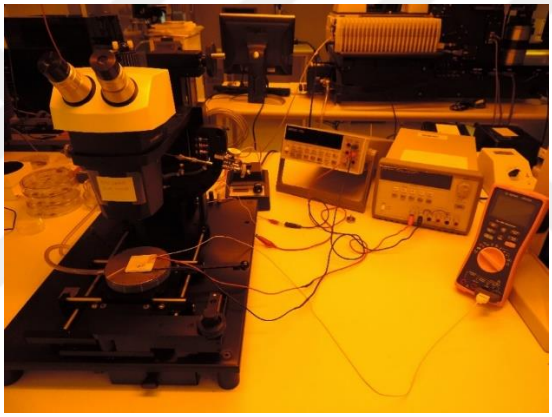

Figure 3.11. TCR measurement setup to monitor resistance values with changing temperature.

Sample temperature is changed between 25 ℃ and 80 ℃. Corresponding resistance values are recorded at 12 different temperature values between 25 ℃ and 80 ℃. The resistivity behavior of V_xO_y thin films change as a function of temperature which is known to obey the Arrhenius relation.[68] Hence, by fitting the resistivity versus temperature data to Arrhenius relation given in Equation 3.4, the activation energy can be extracted.

$$R(T) = R_0 e^{-E_a/kT} \qquad \text{Equation 3.4}$$

here E_a is the activation energy obtained in eV, k is Boltzmann constant which is 8.6173E-5 eV/K, T is the temperature in K, and R_0 is a constant. TCR is then calculated using the activation energy obtained from the fitting in Equation 3.5,

$$TCR = \frac{E_a}{RT^2} \qquad \text{Equation 3.5}$$

Electrical characterization results show that resistivity and TCR values are strongly dependent on the changes in phase ratios caused by V-W co-sputtering. Figure 3.12 shows the change in resistivity values with increasing temperature for the V_xO_y, WO_3-V_xO_y having 5.6% W, and WO_3-V_xO_y having 7.2% W samples between room temperature and 80 °C. With V-W co-sputtering, the resistivities shift significantly to higher values over the entire temperature range.

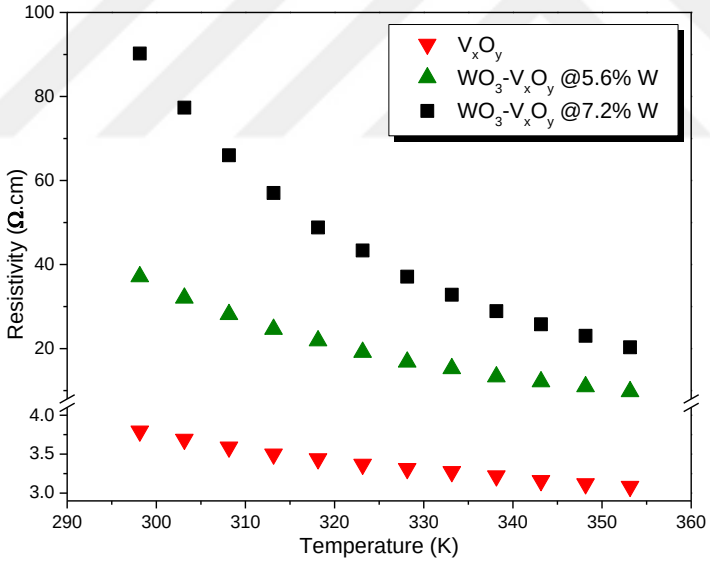

Figure 3.12. Relation of resistivity and temperature for V_xO_y and WO_3-V_xO_y films having 5.6% W, and 7.2% W.

Resistivity of the V_xO_y sample at room temperature is 3.8 ohm.cm and it significantly increases to 90.2 ohm.cm, which is almost a 25-fold increase with only 7.2% W.

Such increase in resistivity values accompanied by V-W co-sputtering relates to the emergence of high resistive V_2O_5 phase, as shown in the structural characterization section.

Resistivities of all samples decreases as the temperature increases and the change is exponential. The resultant fit enables to find the E_a for each sample. Measured resistivities at room temperature are 3.8, 37.1, 90.2 ohm.cm and they decrease to 3.1, 9.8, 20.3 ohm.cm at 80 °C for the V_xO_y, WO_3-V_xO_y with 5.6% W, and WO_3-V_xO_y with 7.2% W concentration, respectively. The resistivity decreases because raising the temperature of a semiconductor will promote the charge carriers to the conduction band and will increase the number of charge carriers which increases conductivity (decreases resistivity). The more charge carriers that are available, the more current a material can conduct. Figure 3.12 also reveals this exponential decrease of resistivity with rising temperature. In comparison to the sharp insulator-to-metal transition (IMT) encountered in VO_2-phase dominant films, this broad transition in resistivity makes the films more suitable for microbolometer applications. The gradual transition rather than an abrupt one prevents the resistivity to suddenly go out of the reading limit of CMOS circuits and provides a microbolometer that can operate in a wide temperature range without a need for temperature control. The microbolometer would work with more or less the same sensitivity over the entire temperature range, and this would be a very significant advantage for the use of microbolometers in TEC-less operations.

The graph in Figure 3.13 presents the temperature dependence of TCRs between room temperature and 80 °C for the V_xO_y and WO_3-V_xO_y samples. In accordance with the resistivity change, the absolute TCRs at each temperature also increase with V-W co-sputtering. Room temperature TCRs are found to be -0.4, -2.9, -3.2 %/K for the V_xO_y, WO_3-V_xO_y with 5.6% W, and WO_3-V_xO_y with 7.2% W concentration, respectively. Therefore, it is shown that V-W co-sputtering results in a remarkable increase in both resistivity and TCR by introducing a new high resistive and high TCR vanadium oxide phase, V_2O_5.

It should be noted here that -0.4 %/K might seem to be a relatively low TCR for V_xO_y because some of the V_xO_y films are known to have TCR values around -2 %/K. However, in all these studies a structural characterization of V_xO_y films formed showed that these relatively high TCR values are due to the presence of high TCR VO_2 and/or V_2O_5 phases in V_xO_y films.[56, 69-72] Since the V_xO_y film in this study does not contain any VO_2 or V_2O_5 phase before co-sputtering, its TCR is relatively low.

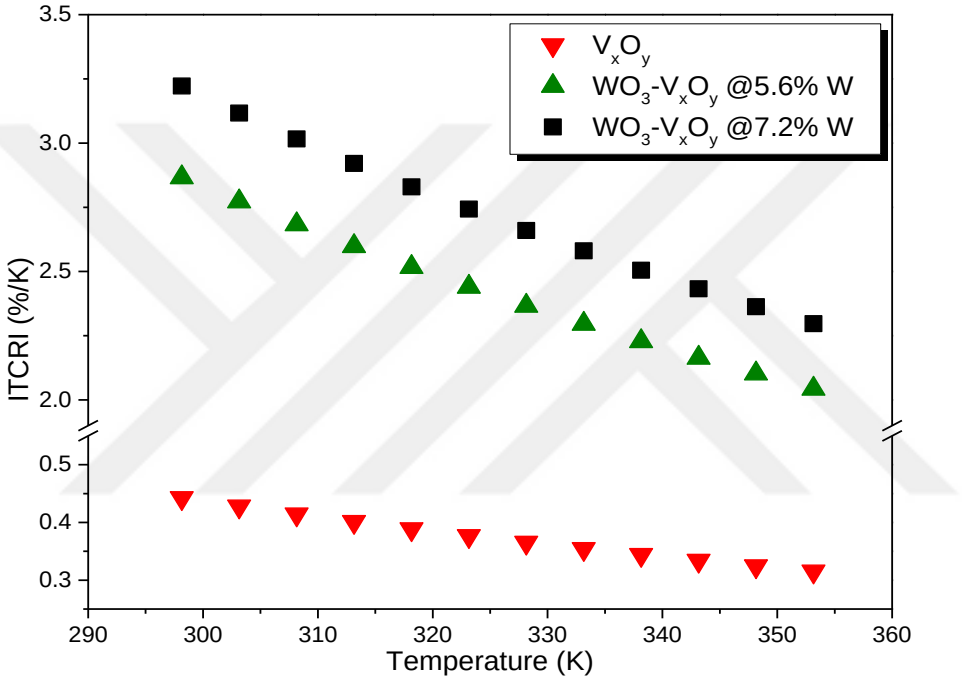

Figure 3.13. Relation of TCR and temperature for V_xO_y and WO_3-V_xO_y films having 5.6% W, and 7.2% W.

Figure 3.14 presents a noise power spectral density of a routinely made pixel structure at METU MEMS Center of a similarly grown film. The active material used in the measured pixel structure is fabricated using the same reactive co-sputtering technique of V and W that is described in this study. The 1/f noise is estimated to be 3.708×10^{-12} and the corner frequency is Details of the noise measurements are given in the reference thesis by Baran Utku Tekin.[57]

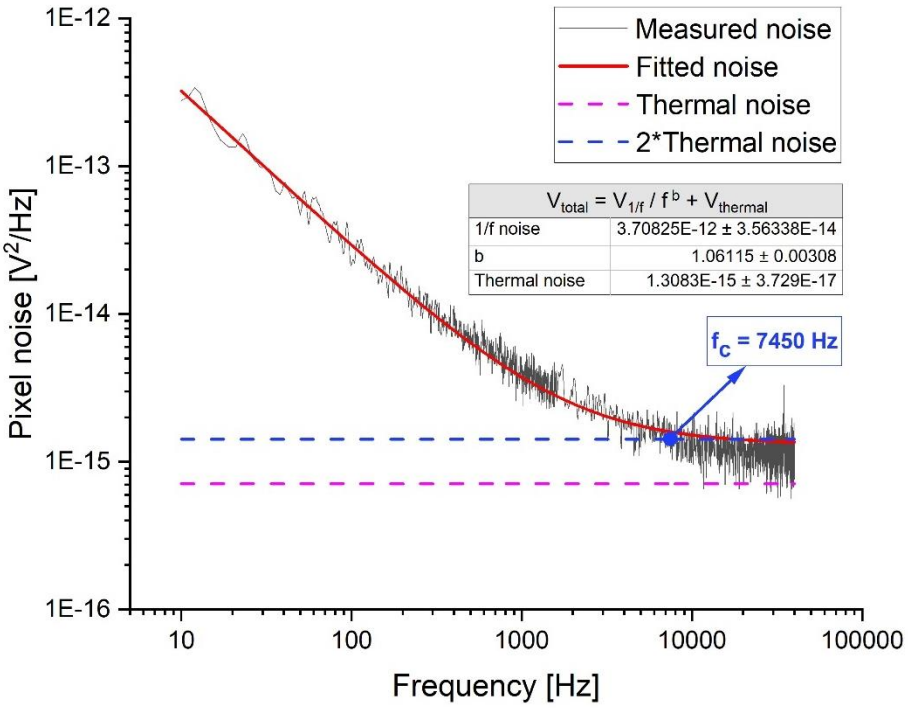

Figure 3.14. The noise power spectral density of a pixel structure having an active material that is fabricated using the same technique described in this study.

3.5 **THz Optical Characterization**

THz optical characterizations are performed using the same setup for TiAlV measurements detailed in Chapter 2. Here, heating the V_xO_y and WO_3-V_xO_y samples up to 80 °C is achieved by using a sample holder with a temperature control unit. Thus, THz-TDS measurements are also achieved as a function of temperature. THz-TDS is being used as a powerful characterization technique for measuring thin film conductivities.[73] Being a contactless technique and thus a non-destructive one makes it superior to contact probe techniques in which the surface of the sample is damaged and contaminated. THz-TDS also provides a significant advantage by allowing conductivity analysis from a large area and from a distance.

The other unique advantage is its ability to monitor the inherent characteristics of samples by providing information on local conductivity effects, which cannot be measured by using conventional probe techniques. Si/Si_xN_y samples are the first evaluated reference samples as in the TiAlV case. 11 sets of measurements are performed for this evaluation, especially for observing the effect of heating the reference sample to different temperatures. In these measurements, the waiting time for reaching the thermal equilibrium at each temperature is optimized, and the effect of purging the sample box is observed. After these optimizations, 5 minutes is given for thermal equilibrium before the measurement at the set temperature, and the sample box is purged to 0% relative humidity prior to the measurement. Figure 3.15 shows the THz time domain profile of the Si/Si_xN_y sample at both 25 °C and 80 °C.

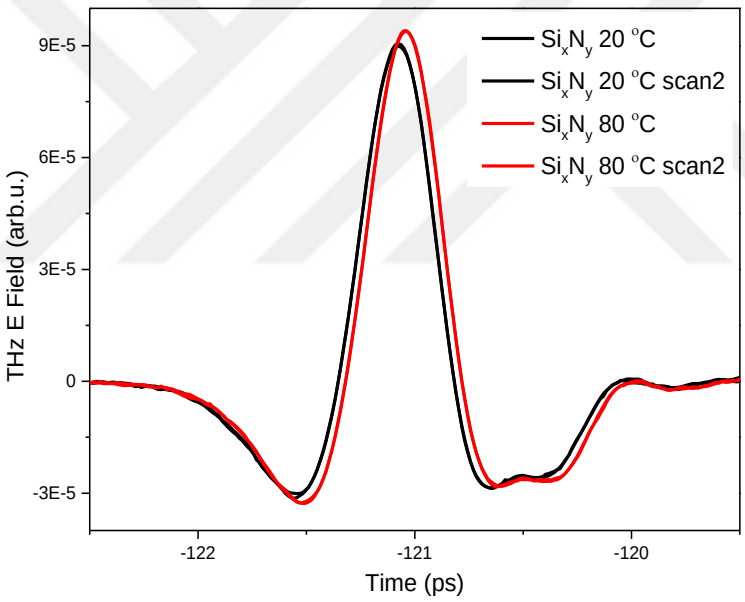

Figure 3.15. Temperature dependent THz time domain profile of Si_xN_y film at 25 °C and 80 °C to be evaluated as a reference.

There is a right shift in time domain as well as an increase in amplitude after increasing the temperature to 80 °C. This behavior of Si/Si_xN_y dominates the time domain profile of the WO_3-V_xO_y sample as can be seen in Figure 3.16.

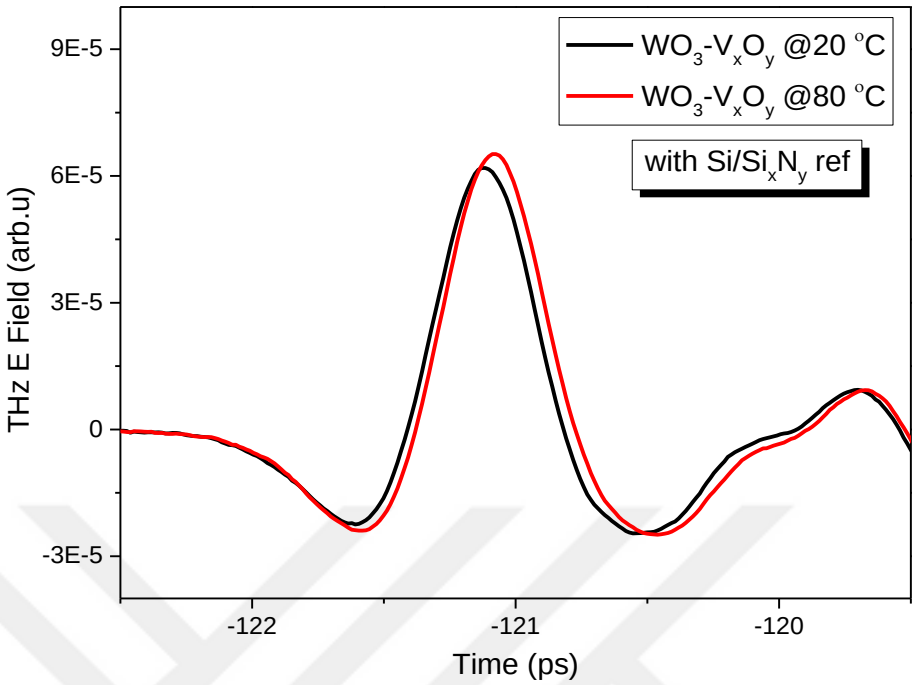

Figure 3.16. THz time domain profiles of WO_3-V_xO_y films on Si/Si_xN_y references at 25 °C and 80 °C.

Therefore, there was a need for determining a substrate that does not change its THz time domain profile as the temperature increases to 80 °C. Although, THz optical insertion losses of the quartz substrates are greater than the Si substrates, quartz substrate with its high temperature stability is a great candidate for such purposes. Figure 3.17 shows the time domain profile of the quartz substrate. There is no difference in time domain profiles measured at room temperature and higher temperatures. Quartz behaves as an ideal reference substrate especially for measurements include heating. Therefore, as mentioned in the Section 3.2, V_xO_y and WO_3-V_xO_y films are deposited on quartz substrates and THz measurements are performed at 25 °C and 80 °C.

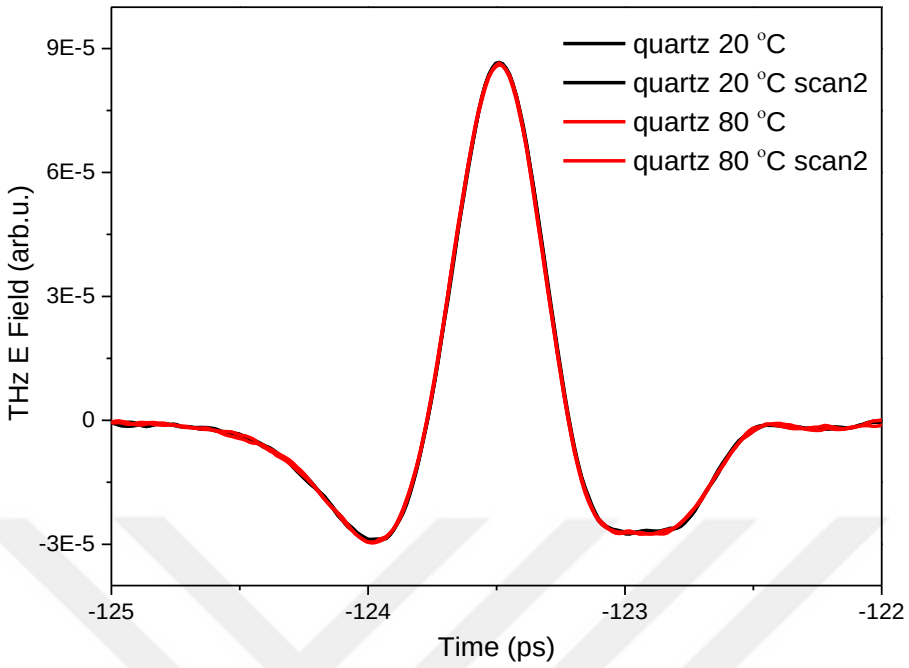

Figure 3.17. THz time domain profile of quartz substrate showing no difference at a higher temperature.

THz measurement conditions are optimized by various trials on heating-cooling cycles of samples. The final optimized procedure is as follows. After the sample is placed on the sample holder and the temperature is set to 25 °C, 5 minutes is given for thermal equilibrium and also for reaching 0% relative humidity in the sample box with continuous purging. The purging is constant with a flow rate low enough not to disturb the measurement. The temperature is then set to 80 °C without opening the sample box after completing the measurement at 25 °C, and again 5 minutes is given for the sample to reach thermal equilibrium. This is followed by cooling the sample back to 25 °C and then heating it to 80 °C again without opening the sample box, and in each case 5 minutes is given for reaching thermal equilibrium. This is done to observe the reproducibility and precision of measurements. Figure 3.18a shows THz time domain profiles of the V_xO_y film exposed to this heating-cooling cycle experiment, and Figure 3.18b shows peak amplitudes in a zoomed-in version.

It is observed that these two measurements at 25 °C overlaps with each other very well. Similarly, two measurements at 80 °C also overlaps well with each other, highlighting the precision and reproducibility of measurements as a function of temperature. It also shows that the changes in V_xO_y films with temperature are reversible.

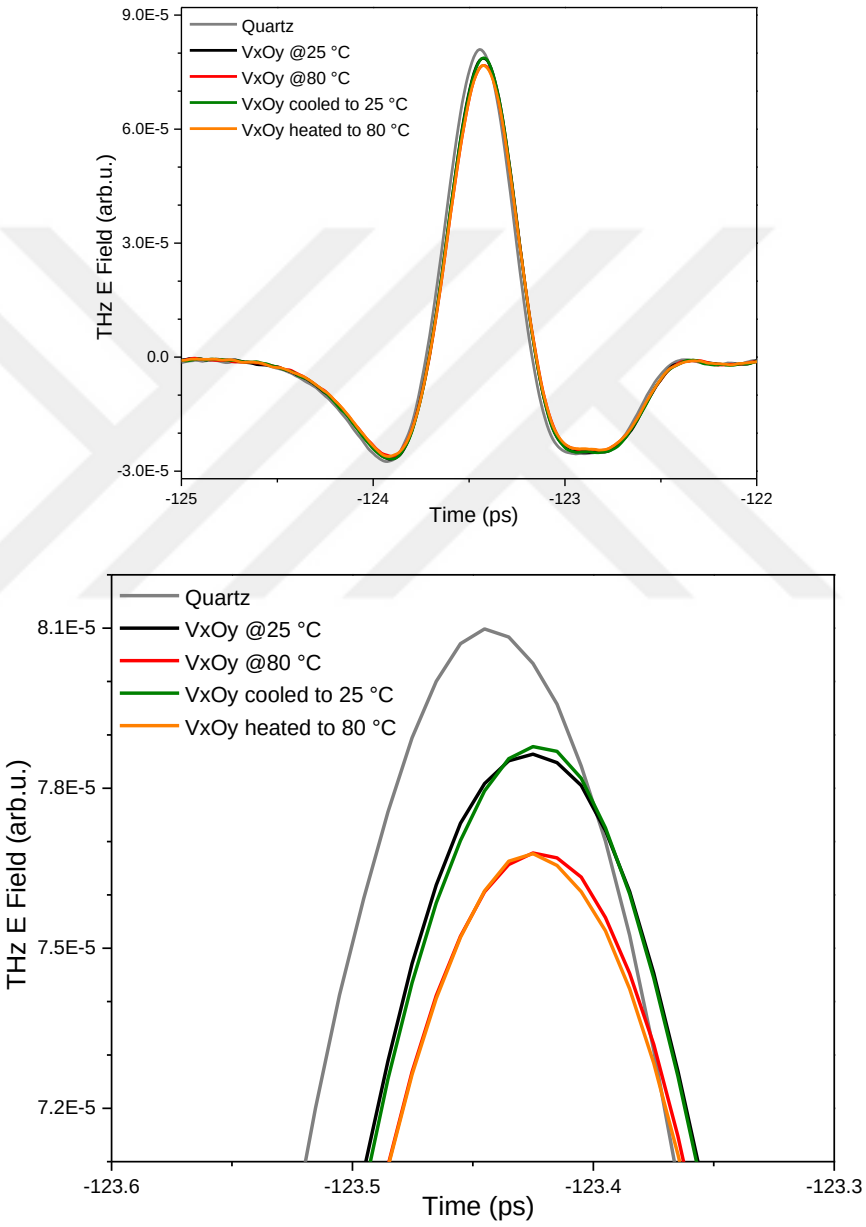

Figure 3.18. a) THz time domain profiles of the V_xO_y film and b) zoomed-in version showing the overlap after the film is exposed to a heating-cooling cycle.

Time domain profiles given in Figure 3.18b shows a decrease in amplitude at 80 °C, but the decrease is not dramatic since fabricated V_xO_y films do not contain VO_2 phase as known from both XPS and electrical results. If VO_2 phase was present, the transmission would decrease dramatically after the IMT at 68 °C.[74] Therefore, films are annealed at 350 °C to make sure they become metallic and observe the corresponding time domain profiles. Figure 3.19 shows how much the amplitude and thus the THz transmission decrease after annealing the sample and making its transition to the metallic phase, which might be useful for future studies.

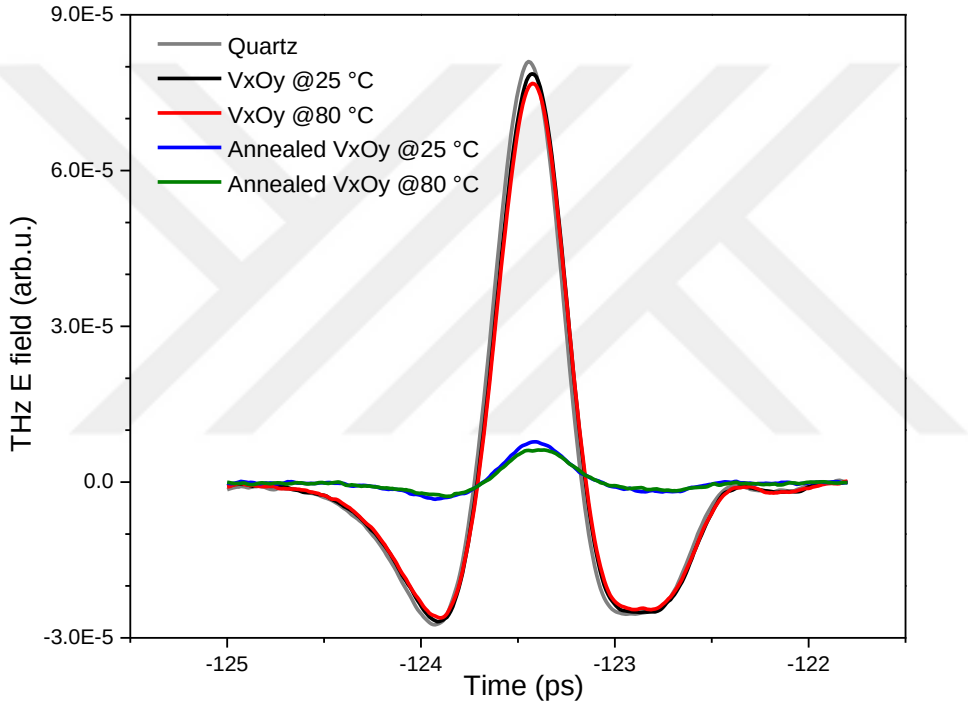

Figure 3.19. The decrease in THz transmission of V_xO_y film after annealing.

After optimizing the heating-cooling measurement conditions and observing the effect of temperature, V_xO_y and WO_3-V_xO_y films having 5.6% W, and 7.2% W concentrations are measured both at 25 °C and 80 °C. Figure 3.20 insets show the corresponding time domain profiles. Expected differences in THz time domain profiles are very small but significant since the difference in W concentrations are also very small. Therefore, it is normal to observe very similar profiles in THz time domain in that scale.

However, differences become clear in the zoomed-in version of graphs. Peak amplitudes showing the significant change in both the time delay and the amplitude with V-W co-sputtering are given in a zoomed-in scale in Figure 3.20.

The quartz substrate is given as a reference and time domain profiles of V_xO_y and WO_3-V_xO_y films having 5.6% W, and 7.2% W are given both at 25 °C (Figure 3.20a) and 80 °C (Figure 3.20b). The first thing to notice here is that there are differences in time domain profiles of all samples meaning that THz-TDS can distinguish the effect of V-W co-sputtering not only between the V_xO_y and WO_3-V_xO_y samples but also between 5.6% W and 7.2% W samples, even though they have only 1.6% difference in their W concentrations. This highlights the extreme sensitivity of THz waves. When these differences are analyzed in detail, there are two effects observed with V-W co-sputtering in Figure 3.20a. Firstly, there is a right shift (delay) in time domain profiles with increasing W concentration. Secondly, the amplitude of THz electric field and thereby the transmission of incoming THz waves gradually decreases with increasing W concentration. The delay in the time domain indicates an increase in refractive index values of the film. On the other hand, the decrease in the THz transmission refers to an increase in local conductivity of films with the electron rich W introduction. At this point, this statement seems to disagree with electrical measurement results at first sight, where resistivities significantly increased, conductivities decreased, with W addition. Here, it should be noted that THz spectroscopy is capable of monitoring the inherent characteristics of samples where probe techniques might be ineffective. For a probe technique to measure a conductivity value, a carrier should move from one electrode to another using the lowest resistive path possible. Thus, probe techniques cannot measure local conductivities of the sample whereas THz waves are extremely sensitive to the changes in local conductivities without any need for a carrier to reach to any electrodes. Thus, monitoring the effects of V-W co-sputtering on local conductivities is possible with THz waves. Resistivities measured with a probe technique show an increase with V-W co-sputtering because the results are dominated by a new high resistive V_2O_5 phase formation.

On the other hand, local conductivities are observed to increase with THz-TDS technique because the results are dominated by the W, being an electron rich element. This highlights the importance of using complementary techniques to understand the material properties thoroughly. Figure 3.20b shows THz time domain profiles at 80 °C where amplitudes and thus THz transmissions are observed to decrease for all samples. The transmission decrease is also shown in THz frequency domain given in Figure 3.21. As mentioned earlier, decrease in the THz transmission indicates an increase in the conductivity. Here, the fact that THz transmission decreases at a higher temperature, support the electrical measurement results where Figure 3.12 showed that resistivities decrease (conductivities increase) at higher temperatures for all samples regardless of the amount of W. On the other hand, V_xO_y sample appears to have a greater temperature dependence since it shows a greater decrease in transmission whereas the WO_3-V_xO_y samples appear to have much less change. This can be attributed to the absence of high resistive V_2O_5 phase in the V_xO_y sample.

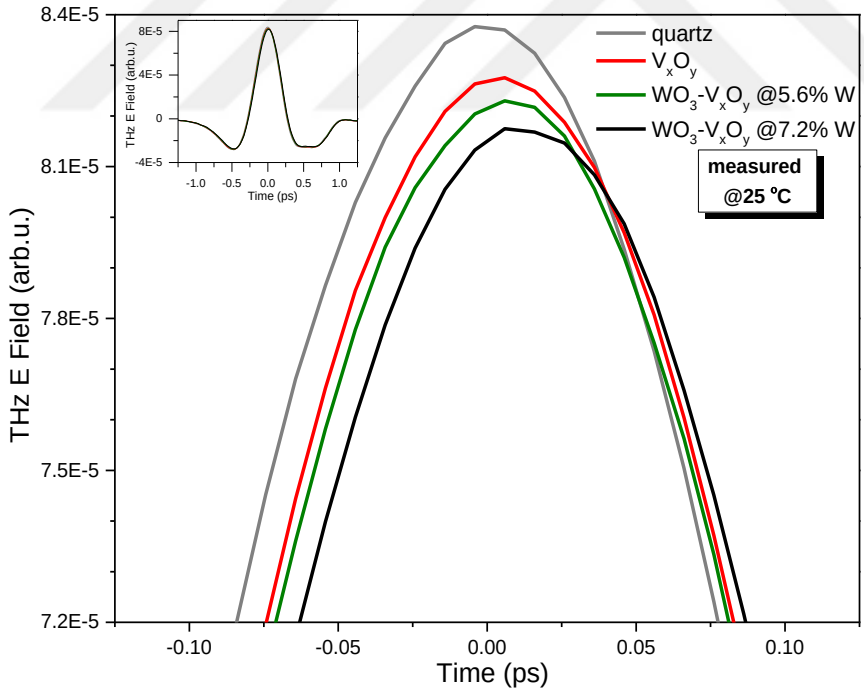

Figure 3.20. THz time domain profiles of quartz reference and V_xO_y and WO_3-V_xO_y films having 5.6% W, and 7.2% W at a) 25 °C and b) 80 °C.

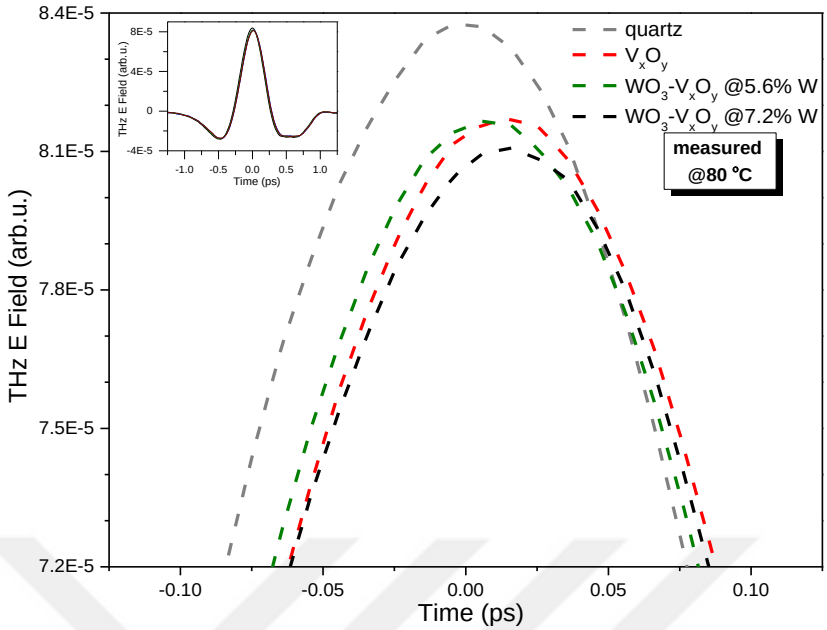

Figure 3.20 (continued). THz time domain profiles of quartz reference and V_xO_y and WO_3-V_xO_y films having 5.6% W, and 7.2% W at a) 25 °C and b) 80 °C.

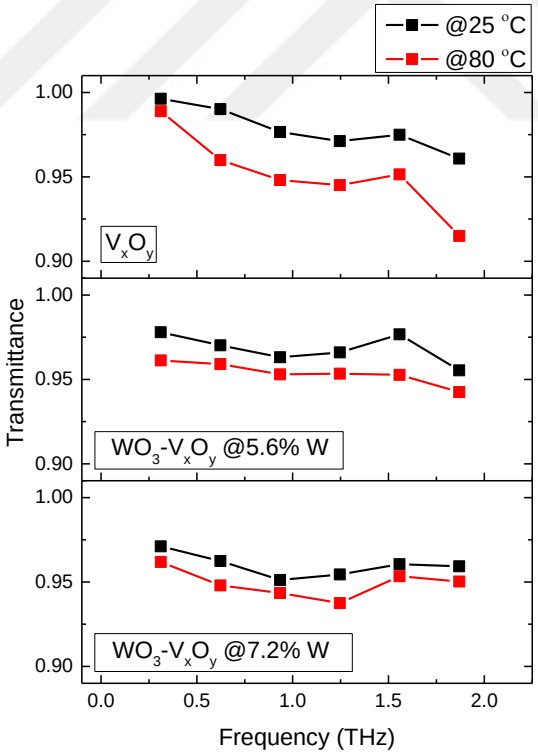

Figure 3.21. Frequency dependent THz transmittances of V_xO_y and WO_3-V_xO_y films having 5.6% W, and 7.2% W at 25 °C and 80 °C.

Tinkham formula [75] given in Equation 3.6 is used to calculate conductivities of V_xO_y and WO_3-V_xO_y thin films at 25 and 80 °C,

$$\frac{\tilde{E}_{f+s}(w)}{\tilde{E}_s(w)} = \frac{1+n_s}{1+n_s+z_0\tilde{\sigma}(w)d} \qquad \text{Equation 3.6}$$

where $\tilde{\boldsymbol{\sigma}}$ is the calculated complex conductivity, $\tilde{\boldsymbol{E}}$ is the complex amplitude of the substrate and subtrate+film, respectively, obtained after FFT analysis of the time domain data, n_s is the refractive index of the substrate, z_0 is the characteristic impedance of free space, and d is the film thickness. Refractive index of the substrate, n_s, that is used in this formula is calculated from the phase difference using Equation 2.8, and Figure 3.22 shows the refractive index of reference quartz substrate in frequency domain, which is consistent with the reported literature values in this frequency range.[76]

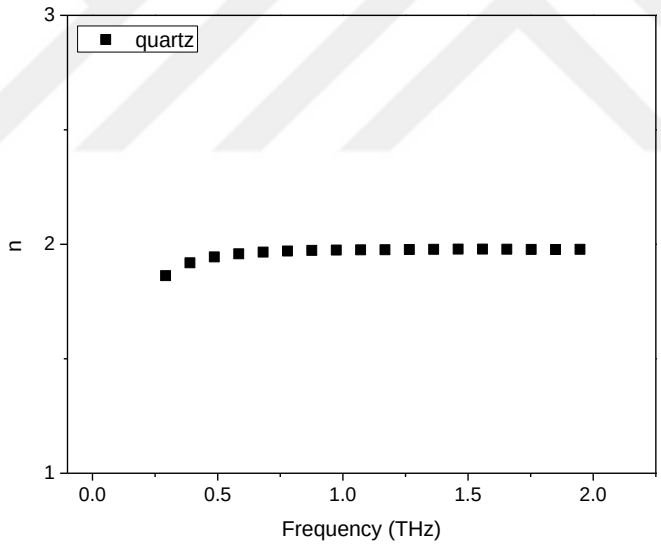

Figure 3.22. Refractive index of the quartz substrate.

Real parts of calculated complex conductivities are given in Figure 3.23 which shows that all the samples have higher conductivities at a higher temperature. This agrees with both electrical measurement results where resistivities have decreased and THz transmission behaviors where the transmission have decreased with increasing temperature.

All the measurement techniques and corresponding calculations support the fact that conductivities of the films increase with increasing temperature which is an expected behavior for all V_xO_y samples being semiconductors.

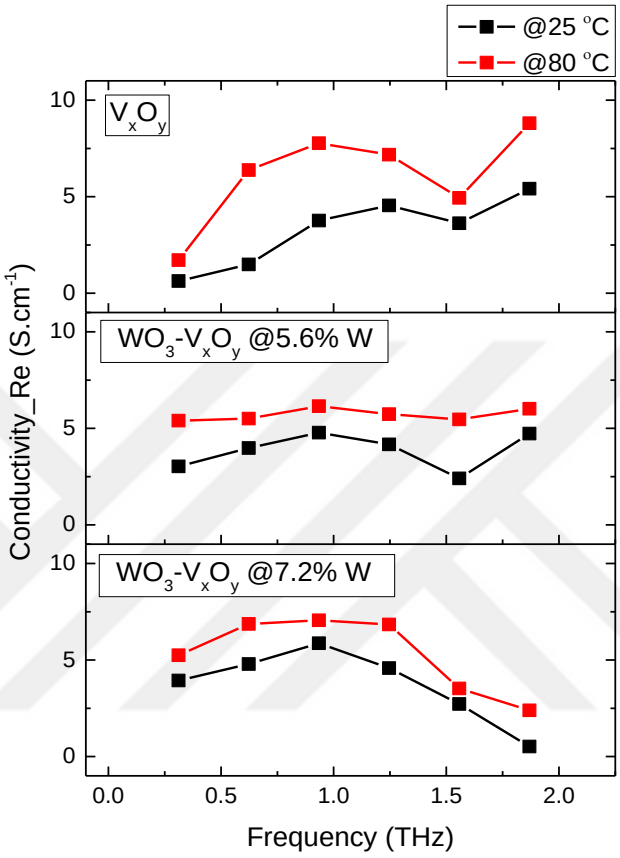

Figure 3.23. Real part of complex conductivities of V_xO_y and WO_3-V_xO_y films having 5.6% W, and 7.2% W at 25 °C and 80 °C.

Imaginary parts of calculated complex conductivities are given in Figure 3.24. At room temperature, WO_3-V_xO_y film having 7.2% W concentration has the highest slope since the slope of imaginary conductivities increases with V-W co-sputtering. The significant difference in these samples is the relative amount of decrease of the V_6O_{13} and V_4O_9 phases while the amounts of V_2O_5 and WO_3 phases increase with V-W co-sputtering. Here, V_2O_5 and WO_3 phases are oxygen rich phases compared to others, and in the literature, oxygen rich phases are associated with deeper electron/carrier trap levels.[77]

After the formation of these oxygen rich V_2O_5 and WO_3 phases, the difference between 25 °C and 80 °C behavior is no longer observed for WO_3-V_xO_y samples, possibly due to significantly low conductivities of samples and deep trapping conditions. On the other hand, a significant amount of change in imaginary conductivity of the V_xO_y sample, having no V_2O_5 or WO_3 phase, is observed as a function of temperature.

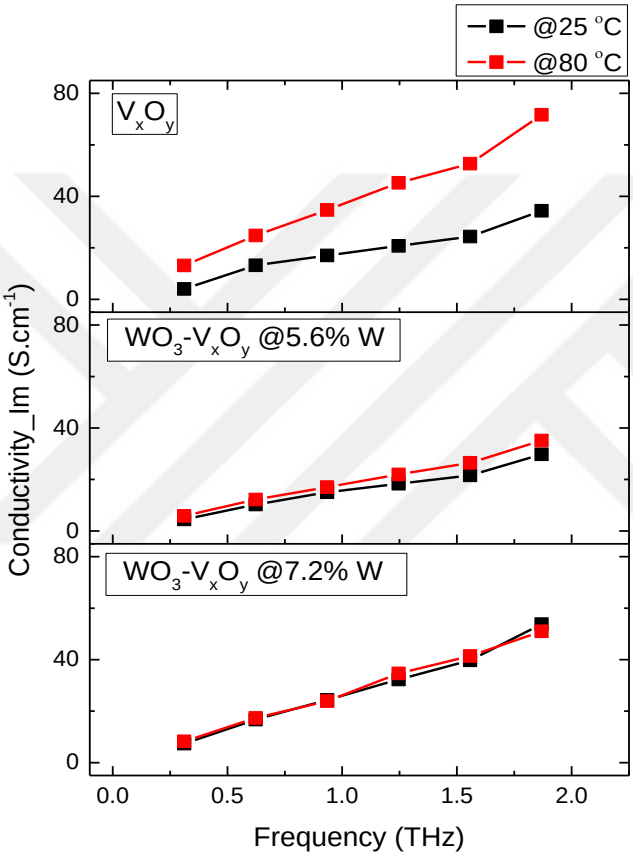

Figure 3.24. Imaginary part of complex conductivities of the V_xO_y and WO_3-V_xO_y films having 5.6% W, and 7.2% W at 25 °C and 80 °C.

Part of the results here are recently published in the reference paper in Journal of Alloys and Compounds.[52] Part of the results are also presented in several international and national conferences such as SPIE Optical Engineering and Applications, 10th International Workshop on Terahertz Technologies and Applications, and 22nd National Optic, Electro-Optic and Photonics Conference.

CHAPTER 4

CONCLUSION

In this study, it is aimed to evaluate and optimize specific properties of absorber and active material layers which are the two critical layers that needs improvement for future THz microbolometers.

Absorber layer studies are started with optimizing the sputtering parameters of the TiAlV target and obtaining a deposition rate to be used in the fabrication of TiAlV layers with desired thicknesses. Absorber layer thickness, sheet resistance, and THz optical measurements are performed to infer the relationship between these parameters. The trend in the loss of incoming THz radiation as a function of sheet resistance, by only changing the absorber layer thickness, is shown to agree with the literature. THz transmissions of all TiAlV layers having different thicknesses are calculated by eliminating the effect of reflection loss. The measured THz transmission values are then subtracted from this reflection corrected transmissions to eliminate the effect of transmission loss too. The resulting values presented the effect of absorption as a function of TiAlV layer thickness. Besides, the effect of surface oxidation is investigated for TiAlV layers with different thicknesses. The amount of increase in sheet resistance especially for thin layers of TiAlV showed the importance of a protection layer. Moreover, experimental sheet resistance values that are obtained using a 4-point probe station are confirmed with a simple calculation using THz-TDS measurement results. This highlights the possible use of THz-TDS as a noncontact and nondestructive alternative to probe techniques. Finally, the trade-off between absorption and the foreseen speed of the THz microbolometer is discussed in terms of time constant, to choose a convenient absorber layer thickness.

In active material layer studies, a fabrication method is proposed to solve the one of the most challenging issues of active material layers, which is to be able to stay in the resistivity range for CMOS applications while maintaining a high TCR and a low noise. Here, it is presented that with a simple co-sputtering of V and W at room temperature, one can control the formed phases of the V_xO_y films that contain different ratios of pure phases. With this deposition approach, individual phases and their concentrations are controlled by V-W reactive co-sputtering, which enabled the control of the resultant resistivity and TCR. Exploration of the control of this behavior is essential for fabrication of a high TCR film with a compatible resistivity. In addition, besides the classical characterization techniques, a new complementary noncontact THz-TDS technique is introduced for the characterization of V_xO_y and WO_3-V_xO_y films for the first time. THz-TDS offers new insights especially about the changes in local conductivities with V-W co-sputtering as well as with temperature. This thesis introduces THz-TDS as a promising tool for future inline characterization of conductivity of these V_xO_y thin films by presenting the first ever non-contact measurements of these mixed phase films.

The studies presented here might be extended toward the following directions;

- Different metals can be deposited aiming the same layer thickness and then aiming the same sheet resistance value for all metals. These two sets of samples can be characterized using THz-TDS to understand the effect of the type of the metal itself.
- Increased W sputtering powers can be evaluated to reach the maximum TCR in the required resistivity range. Detailed noise measurements should be performed for high TCR samples to choose the right W level with a compatible noise.
- Both TiAlV as the absorber layer and WO_3-V_xO_y as the active material layer can be incorporated in a test pixel structure with convenient IR blocking, before a CMOS-application.

REFERENCES

[1] D. Dragoman and M. Dragoman, “Terahertz fields and applications,” *Prog. Quantum Electron.*, vol. 28, no. 1, pp. 1–66, Jan. 2004, doi: 10.1016/S0079-6727(03)00058-2.

[2] L. Popa-Simil, “Multi-band Terahertz Imaging System Design,” *MRS Proc.*, vol. 872, p. J15.3, Feb. 2005, doi: 10.1557/PROC-872-J15.3.

[3] H. Guerboukha, K. Nallappan, and M. Skorobogatiy, “Toward real-time terahertz imaging,” *Adv. Opt. Photonics*, vol. 10, no. 4, p. 843, Dec. 2018, doi: 10.1364/AOP.10.000843.

[4] L. Wei, L. Yu, H. Jiaoqi, H. Guorong, Z. Yang, and F. Weiling, “Application of terahertz spectroscopy in biomolecule detection,” *Front. Lab. Med.*, vol. 2, no. 4, pp. 127–133, Dec. 2018, doi: 10.1016/j.flm.2019.05.001.

[5] K. Kawase, Y. Ogawa, Y. Watanabe, and H. Inoue, “Non-destructive terahertz imaging of illicit drugs using spectral fingerprints,” *Opt. Express*, vol. 11, no. 20, p. 2549, Oct. 2003, doi: 10.1364/OE.11.002549.

[6] I. E. Carranza, J. P. Grant, J. Gough, and D. Cumming, “Terahertz metamaterial absorbers implemented in CMOS technology for imaging applications: Scaling to large format focal plane arrays,” *IEEE J. Sel. Top. Quantum Electron.*, vol. 23, no. 4, 2017, doi: 10.1109/JSTQE.2016.2630307.

[7] P. Zolliker, M. Shalaby, E. Söllinger, E. Mavrona, and E. Hack, “Real-Time High Resolution THz Imaging with a Fiber-Coupled Photo Conductive Antenna and an Uncooled Microbolometer Camera,” *Sensors*, vol. 21, no. 11, p. 3757, May 2021, doi: 10.3390/s21113757.

[8] A. Nguyen, “Biomedical imaging with THz waves,” *Heal. Monit. Struct. Biol. Syst. 2010*, vol. 7650, p. 76503D, 2010, doi: 10.1117/12.847073.

[9] Z. D. Taylor, R.S. Singh, D. B. Bennett, P. Tewari, C. P. Kealey, N. Bajwa, M. O. Culjat, A. Stojadinovic, H. Lee, J. Hubschman, E. R. Brown, and W. S. Grundfest, “THz Medical Imaging: in vivo Hydration Sensing,” *IEEE Trans. Terahertz Sci. Technol.*, vol. 1, no. 1, pp. 201–219, Sep. 2011, doi: 10.1109/TTHZ.2011.2159551.

[10] A. Rogalski, “History of infrared detectors,” *Opto-Electronics Rev.*, vol. 20, no. 3, pp. 77–85, Jan. 2012, doi: 10.2478/s11772-012-0037-7.

[11] A. Rogalski, “Next decade in infrared detectors,” in *Electro-Optical and Infrared Systems: Technology and Applications XIV*, Oct. 2017, no. October 2017, p. 100, doi: 10.1117/12.2300779.

[12] M. Y. Tanrıkulu, “An Uncooled Infrared Microbolometer Detector Array Using Surface Micromachined MEMS Technology,” Dissertation for the Degree of Doctor of Philosophy, Middle East Technical University, 2007.

[13] M. Kohin and N. R. Butler, “Performance limits of uncooled VO x microbolometer focal plane arrays,” in *Infrared Technology and Applications XXX*, Aug. 2004, vol. 5406, no. January, p. 447, doi: 10.1117/12.542482.

[14] D. Murphy, M. Ray, J. Wyles, C. Hewitt, R. Wyles, E. Gordon, K. Almada, T. Sessler, S. Baur, D. Van Lue, and S. Black, “640 × 512 17 μm microbolometer FPA and sensor development,” in *Infrared Technology and Applications XXXIII*, Apr. 2007, vol. 6542, p. 65421Z, doi: 10.1117/12.724345.

[15] C. Li, C. J. Han, and G. Skidmore, “Overview of DRS uncooled VOx infrared detector development,” *Opt. Eng.*, vol. 50, no. 6, p. 061017, Jun. 2011, doi: 10.1117/1.3593155.

[16] F. Niklaus, C. Vieider, and H. Jakobsen, “MEMS-based uncooled infrared bolometer arrays: a review,” *MEMS/MOEMS Technol. Appl. III*, vol. 6836, no. January 2008, p. 68360D, 2007, doi: 10.1117/12.755128.

[17] A. W. Lee and Q. Hu, “Real-time, continuous-wave terahertz imaging by use of a microbolometer focal-plane array,” *Opt. Lett.*, vol. 30, no. 19, p. 2563, Oct. 2005, doi: https://doi.org/10.1364/OL.30.002563.

[18] A. W. M. Lee, B. S. Wil, S. Kumar, Qing Hu, and J. L. Reno, “Real-time imaging using a 4.3-THz quantum cascade laser and a 320x240 microbolometer focal-plane array,” *IEEE Photonics Technol. Lett.*, vol. 18, no. 13, pp. 1415–1417, Jul. 2006, doi: 10.1109/LPT.2006.877220.

[19] N. Oda, H. Yoneyama, T. Sasaki, M. Sano, S. Kurashina, I. Hosako, N. Sekine, T. Sudoh, and T. Irie, “Detection of terahertz radiation from quantum cascade laser using vanadium oxide microbolometer focal plane arrays,” *Infrared Technol. Appl. XXXIV*, vol. 6940, no. May 2008, p. 69402Y, 2008, doi: 10.1117/12.781630.

[20] N. Oda, “Uncooled bolometer-type Terahertz focal plane array and camera for real-time imaging,” *Comptes Rendus Phys.*, vol. 11, no. 7–8, pp. 496–509, Aug. 2010, doi: 10.1016/j.crhy.2010.05.001.

[21] J. Gou, J. Wang, W. Li, H. Tai, D. Gu, and Y. Jiang, “Terahertz Absorption Characteristics of NiCr Film and Enhanced Absorption by Reactive Ion Etching in a Microbolometer Focal Plane Array,” *J. Infrared, Millimeter, Terahertz Waves*, vol. 34, no. 7–8, pp. 431–436, Aug. 2013, doi: 10.1007/s10762-013-9992-4.

[22] J. Gou, J. Wang, X. Zheng, D. Gu, H. Yu, and Y. Jiang, “Detection of terahertz radiation from 2.52 THz CO2 laser using a 320 × 240 vanadium oxide microbolometer focal plane array,” *RSC Adv.*, vol. 5, no. 102, pp. 84252–84256, 2015, doi: 10.1039/c5ra15049c.

[23] N. Nemoto, N. Kanda, R. Imai, K. Konishi, M. Miyoshi, S. Kurashina, T. Sasaki, N. Oda, and M. Kuwata-Gonokami, “High-Sensitivity and Broadband, Real-Time Terahertz Camera Incorporating a Micro-Bolometer Array with Resonant Cavity Structure,” *IEEE Trans. Terahertz Sci. Technol.*, vol. 6, no. 2, pp. 175–182, Mar. 2016, doi: 10.1109/TTHZ.2015.2508010.

[24] F. Simoens, L. Dussopt, J. Meilhan, J. Nicolas, N. Monnier, A. Siligaris, B. Hiberty, J. Perraud, P. Mounaix, J. Lalanne-Dera, and O. Redon, “Towards industrial applications of terahertz real-time imaging,” in *Terahertz, RF, Millimeter, and Submillimeter-Wave Technology and Applications XI*, Mar. 2018, no. March 2018, p. 29, doi: 10.1117/12.2287709.

[25] N. Oda, “Technology trend in real-time, uncooled image sensors for sub-THz and THz wave detection,” in *Micro- and Nanotechnology Sensors, Systems, and Applications VIII*, May 2016, vol. 9836, p. 98362P, doi: 10.1117/12.2222290.

[26] F. Simoens, J. Meilhan, and J.-A. Nicolas, “Terahertz Real-Time Imaging Uncooled Arrays Based on Antenna-Coupled Bolometers or FET Developed at CEA-Leti,” *J. Infrared, Millimeter, Terahertz Waves*, vol. 36, no. 10, pp. 961–985, Oct. 2015, doi: 10.1007/s10762-015-0197-x.

[27] D. Dufour, L. Marchese, M. Terroux, H. Oulachgar, F. Généreux, M. Doucet, L. Mercier, B. Tremblay, C. Alain, P. Beaupré, N. Blanchard, M. Bolduc, C. Chevalier, D. D’Amato, Y. Desroches, F. Duchesne, L. Gagnon, S. Ilias, H. Jerominek, F. Lagacé, J. Lambert, F. Lamontagne, L. Le Noc, A. Martel, O. Pancrati, J. Paultre, T. Pope, F. Provençal, P. Topart, C. Vachon, S. Verreault, and A. Bergeron, “Review of terahertz technology development at INO,” *J. Infrared, Millimeter, Terahertz Waves*, vol. 36, no. 10, pp. 922–946, Oct. 2015, doi: 10.1007/s10762-015-0181-5.

[28] G. Valušis, A. Lisauskas, H. Yuan, W. Knap, and H. G. Roskos, “Roadmap of Terahertz Imaging 2021,” *Sensors*, vol. 21, no. 12, p. 4092, Jun. 2021, doi: 10.3390/s21124092.

[29] S. Liu and Y. C. Shin, “Additive manufacturing of Ti6Al4V alloy: A review,” *Mater. Des.*, vol. 164, p. 107552, Feb. 2019, doi: 10.1016/j.matdes.2018.107552.

[30] J. J. Rausch, F. A. Crossley, and H. D. Kessler, “Titanium-Rich Corner of the Ti-AI-V System,” *J. Met.*, pp. 211–214, 1956.

[31] R. Pederson, “Microstructure and Phase Transformation of Ti-6Al-4V,” Lulea University of Technology, 2002.

[32] Z. Liu and G. Welsch, “Literature Survey on Diffusivities of Oxygen, Aluminum, and Vanadium in Alpha Titanium, Beta Titanium, and in Rutile,” *Metall. Trans. A*, vol. 19, no. 4, pp. 1121–1125, Apr. 1988, doi: 10.1007/BF02628396.

[33] A. Baptista, F. Silva, J. Porteiro, J. Míguez, and G. Pinto, “Sputtering Physical Vapour Deposition (PVD) Coatings: A Critical Review on Process Improvement and Market Trend Demands,” *Coatings*, vol. 8, no. 11, p. 402, Nov. 2018, doi: 10.3390/coatings8110402.

[34] J. M. Quero, F. Perdigones, and C. Aracil, “Microfabrication technologies used for creating smart devices for industrial applications,” in *Smart Sensors and MEMs*, Elsevier, 2018, pp. 291–311.

[35] H. M. Cothrel, “Photolithography for the Investigation of Nanostructures,” Honors Tutorial College, Ohio University, 2015.

[36] Ş. E. Küçük, M. Yusuf Tanrıkulu, and T. Akın, “A detailed analysis for the absorption coefficient of multilevel uncooled infrared detectors,” in *Infrared Technology and Applications XXXVII*, May 2011, vol. 8012, no. 1, p. 80121R, doi: 10.1117/12.890236.

[37] J. Krupka, “Contactless methods of conductivity and sheet resistance measurement for semiconductors, conductors and superconductors,” *Meas. Sci. Technol.*, vol. 24, no. 6, p. 062001, Jun. 2013, doi: 10.1088/0957-0233/24/6/062001.

[38] P. H. Q. Pham, W. Zhang, N. H. Quach, J. Li, W. Zhou, D. Scarmardo, E. R. Brown, and P. J. Burke, “Broadband impedance match to two-dimensional materials in the terahertz domain,” *Nat. Commun.*, vol. 8, no. 1, 2017, doi: 10.1038/s41467-017-02336-z.

[39] Y. Zhou, X. Xu, F. Hu, X. Zheng, W. Li, P. Zhao, J. Bai, and Z. Ren, “Graphene as broadband terahertz antireflection coating,” *Appl. Phys. Lett.*, vol. 104, no. 5, pp. 1–6, 2014, doi: 10.1063/1.4863838.

[40] Y. S. Aytekin, “Time Domain Terahertz Spectroscopy: Construction of the Setup and Application in Analysis of Active Pharmaceutical Ingredients,” Middle East Technical University, 2016.

[41] E. Arık, H. Altan, and O. Esentürk, “Dielectric Properties of Diesel and Gasoline by Terahertz Spectroscopy,” *J. Infrared, Millimeter, Terahertz Waves*, vol. 35, no. 9, pp. 759–769, Sep. 2014, doi: 10.1007/s10762-014-0081-0.

[42] A. J. Syllaios, M. J. Ha, W. L. McCardel, and T. R. Schimert, “Measurement of thermal time constant of microbolometer arrays,” in *Infrared Technology and Applications XXXI*, May 2005, vol. 5783, p. 625, doi: 10.1117/12.603153.

[43] R. Çetin and O. Ertürk, “Subwavelength perforated absorbers for infrared detectors,” *Opt. Express*, vol. 28, no. 22, p. 33699, Oct. 2020, doi: 10.1364/OE.405100.

[44] J. Jung, K. Song, J. Choi, J. Lee, D. Choi, J. Jeong, and D. P. Neikirk, "Infrared broadband metasurface absorber for reducing the thermal mass of a microbolometer," *Sci. Rep.*, vol. 7, no. 1, p. 430, Dec. 2017, doi: 10.1038/s41598-017-00586-x.

[45] C. Li, C. J. Han, G. D. Skidmore, G. Cook, K. Kubala, R. Bates, D. Temple, J. Lannon, A. Hilton, K. Glukh, and B. Hardy, " Low-cost uncooled VO x infrared camera development ," *Infrared Technol. Appl. XXXIX*, vol. 8704, p. 87041L, 2013, doi: 10.1117/12.2019653.

[46] J. Lee, C. Rodriguez, and R. Blackwell, "BAE Systems' 17mm LWIR camera core for civil, commercial, and military applications," *Infrared Technol. Appl. XXXIX*, vol. 8704, p. 87041J, 2013, doi: 10.1117/12.2018090.

[47] C. M. Hanson, S. Ajmera, J. Brady, T. Fagan, W. McCardel, D. Morgan, T. Schimert, A. J. Syllaios, and M. F. Taylor, "Small pixel a-Si/a-SiGe bolometer focal plane array technology at L-3 Communications," *Infrared Technol. Appl. XXXVI*, vol. 7660, p. 76600R, 2010, doi: 10.1117/12.852511.

[48] S. Becker, P. Imperinetti, J. Yon, J. Ouvrier-Buffet, V. Goudon, A. Hamelin, C. Vialle, and A. Arnaud, "Latest pixel size reduction of uncooled IR-FPA at CEA, LETI," in *Electro-Optical and Infrared Systems: Technology and Applications IX*, Oct. 2012, vol. 8541, p. 85410C, doi: 10.1117/12.974579.

[49] B. Kebapçı, "Development of High Performance Uncooled Infrared Detector Materials," Middle East Technical University, 2011.

[50] Ö. Dervişoğlu, "A Microbolometer Detector Based on a Sol-Gel Technology," Middle East Technical University, 2013.

[51] N. Eroğlu, "Development of High Performance Active Materials for Microbolometers," Middle East Technical University, 2011.

[52] B. Atik, E. Dirican, O. Demirörs, H. Altan, O. Esentürk, M. Yıldırım, and T. Akın, "Tuning structural, electrical, and THz optical properties of VxOy films with W-doping," *J. Alloys Compd.*, vol. 903, p. 163922, May 2022, doi: 10.1016/j.jallcom.2022.163922.

[53] R. A. Wood, "Uncooled thermal imaging with monolithic silicon focal planes," in *Proceedings of SPIE, Infrared Technology XIX*, Nov. 1993, vol. 2020, no. November 1993, p. 322, doi: 10.1117/12.160553.

[54] R. A. Wood, "United States Patent (19)," US00RE36615E, 1993.

[55] C. Venkatasubramanian, O. M. Cabarcos, D. L. Allara, M. W. Horn, and S. Ashok, "Correlation of temperature response and structure of annealed VOx thin films for IR detector applications," *J. Vac. Sci. Technol. A Vacuum, Surfaces, Film.*, vol. 27, no. 4, pp. 956–961, Jul. 2009, doi: 10.1116/1.3143667.

[56] A. Subrahmanyam, Y. Bharat Kumar Reddy, and C. L. Nagendra, "Nano-vanadium oxide thin films in mixed phase for microbolometer applications," *J. Phys. D. Appl. Phys.*, vol. 41, no. 19, 2008, doi: 10.1088/0022-3727/41/19/195108.

[57] B. U. Tekin, "Development of Small Size Uncooled Infrared Microbolometer Pixel," Middle East Technical University, 2021.

[58] T. Akın, "CMOS-based Thermal Sensors," in *Advanced Micro and Nanosystems*, vol. 2, pp. 479–512, 2005.

[59] G. Silversmit, D. Depla, H. Poelman, G. B. Marin, and R. De Gryse, "An XPS study on the surface reduction of V2O5(001) induced by Ar+ ion bombardment," *Surf. Sci.*, vol. 600, no. 17, pp. 3512–3517, Sep. 2006, doi: 10.1016/j.susc.2006.07.006.

[60] J. Mendialdua, R. Casanova, and Y. Barbaux, “XPS studies of V2O5, V6O13, VO2 and V2O3,” *J. Electron Spectros. Relat. Phenomena*, vol. 71, no. 3, pp. 249–261, Apr. 1995, doi: 10.1016/0368-2048(94)02291-7.

[61] G. Silversmit, D. Depla, H. Poelman, G. B. Marin, and R. De Gryse, “Determination of the V2p XPS binding energies for different vanadium oxidation states (V5+ to V0+),” *J. Electron Spectros. Relat. Phenomena*, vol. 135, no. 2–3, pp. 167–175, Apr. 2004, doi: 10.1016/j.elspec.2004.03.004.

[62] S.-E. Chen, H.-H. Lu, S. Brahma, and J.-L. Huang, “Effects of annealing on thermochromic properties of W-doped vanadium dioxide thin films deposited by electron beam evaporation,” *Thin Solid Films*, vol. 644, pp. 52–56, Dec. 2017, doi: 10.1016/j.tsf.2017.05.052.

[63] R. Lindström, V. Maurice, S. Zanna, L. Klein, H. Groult, L. Perrigaud, C. Cohen, and P. Marcus, “Thin films of vanadium oxide grown on vanadium metal: oxidation conditions to produce V2O5 films for Li-intercalation applications and characterisation by XPS, AFM, RBS/NRA,” *Surf. Interface Anal.*, vol. 38, no. 1, pp. 6–18, Jan. 2006, doi: 10.1002/sia.2141.

[64] W. Burkhardt, T. Christmann, B. Meyer, W. Niessner, D. Schalch, and A. Scharmann, “W- and F-doped VO 2 films studied by photoelectron spectrometry,” *Thin Solid Films*, vol. 345, no. 2, pp. 229–235, May 1999, doi: 10.1016/S0040-6090(98)01406-0.

[65] M. Demeter, M. Neumann, and W. Reichelt, “Mixed-valence vanadium oxides studied by XPS,” *Surf. Sci.*, vol. 454–456, no. 1, pp. 41–44, May 2000, doi: 10.1016/S0039-6028(00)00111-4.

[66] X. Dong, Z. Wu, X. Xu, T. Wang, and Y. Jiang, “Effects of duty cycle and oxygen flow rate on the formation and properties of vanadium oxide films deposited by pulsed reactive sputtering,” *Vacuum*, vol. 104, pp. 97–104, Jun. 2014, doi: 10.1016/j.vacuum.2014.01.020.

[67] W. Li, J. Gou, J. Wang, and X. Wei, “Improving the wet chemical patterning of nichrome film by inserting an ultrathin titanium layer,” *AIP Adv.*, vol. 6, no. 12, p. 125309, Dec. 2016, doi: 10.1063/1.4968177.

[68] H. M. R. Giannetta, C. Calaza, L. Fraigi, and L. Fonseca, “Vanadium Oxide Thin Films Obtained by Thermal Annealing of Layers Deposited by RF Magnetron Sputtering at Room Temperature,” in *Modern Technologies for Creating the Thin-film Systems and Coatings*, 1st ed., Nikolay Nikitenkov, Ed. InTech, 2017, pp. 151–168.

[69] H. Wang, X. Yi, and S. Chen, “Low temperature fabrication of vanadium oxide films for uncooled bolometric detectors,” *Infrared Phys. Technol.*, vol. 47, no. 3, pp. 273–277, 2006, doi: 10.1016/j.infrared.2005.04.001.

[70] J. Dai, X. Wang, S. He, Y. Huang, and X. Yi, “Low temperature fabrication of VOx thin films for uncooled IR detectors by direct current reactive magnetron sputtering method,” *Infrared Phys. Technol.*, vol. 51, no. 4, pp. 287–291, 2008, doi: 10.1016/j.infrared.2007.12.002.

[71] H. Y. Lee, C. Wu, C. Kao, C. Lee, S. Tang, W. Lin, H. Chen, and J. Lin, “Investigated performance of uncooled tantalum-doped VO x floating-type microbolometers,” *Appl. Surf. Sci.*, vol. 354, pp. 106–109, 2015, doi: 10.1016/j.apsusc.2015.03.008.

[72] T.-H. Yeh, C.-K. Tsai, S.-Y. Chu, H.-Y. Lee, and C.-T. Lee, “ Performance improvement of Y-doped VO x microbolometers with nanomesh antireflection layer ,” *Opt. Express*, vol. 28, no. 5, p. 6433, 2020, doi: 10.1364/oe.386438.

[73] N. Laman and D. Grischkowsky, “Terahertz conductivity of thin metal films,” *Appl. Phys. Lett.*, vol. 93, no. 5, p. 051105, Aug. 2008, doi: 10.1063/1.2968308.

[74] C. Ji, Z. Wu, X. Wu, H. Feng, J. Wang, Z. Huang, H. Zhou, W. Yao, J. Gou, and Y. Jiang, “Optimization of metal-to-insulator phase transition properties in polycrystalline VO 2 films for terahertz modulation applications by doping,” *J. Mater. Chem. C*, vol. 6, no. 7, pp. 1722–1730, 2018, doi: 10.1039/C7TC05536F.

[75] R. E. Glover and M. Tinkham, “Conductivity of Superconducting Films for Photon Energies between 0.3 and 40 kT,” *Phys. Rev.*, vol. 108, no. 2, pp. 243–256, Oct. 1957, doi: 10.1103/PhysRev.108.243.

[76] M. Naftaly and R. E. Miles, “Terahertz Time-Domain Spectroscopy for Material Characterization,” *Proc. IEEE*, vol. 95, no. 8, pp. 1658–1665, Aug. 2007, doi: 10.1109/JPROC.2007.898835.

[77] J. Strand, M. Kaviani, D. Gao, A.-M. El-Sayed, V. V Afanas’ev, and A. L. Shluger, “Intrinsic charge trapping in amorphous oxide films: status and challenges,” *J. Phys. Condens. Matter*, vol. 30, no. 23, p. 233001, Jun. 2018, doi: 10.1088/1361-648X/aac005.